# Numerical and experimental investigation of enhancing transdermal model drug delivery: a study on bio-inspired microneedles and iontophoresis integration

By

Mahsa Madadi Masouleh

B.Sc., University of Zanjan, Iran

A Thesis Submitted in Partial Fulfillment of the Requirements for the Degree of

Master of Applied Science

in the Department of Electrical Engineering



University of Victoria

*Numerical and experimental investigation of enhancing transdermal model drug delivery: a study on bio-inspired microneedles and iontophoresis integration*

submitted by Mahsa Madadi Masouleh in partial fulfilment of the requirements for the degree of Master of Applied Science in Electrical Engineering.

**Examining Committee:**

**Supervisor**

Dr. Mina Hoorfar, Faculty of Engineering and Computer Science

**Outside Member**

Dr. Mohsen Akbari, Faculty of Mechanical Engineering

## Abstract

This study investigates the potential enhancement in model drug (acid/dye) delivery by integrating microneedle (MN) technology with iontophoresis (ITP), focusing on transitioning from cone-shaped MNs to bio-inspired variants. It aims to assess the influence of altering MN geometry, particularly incorporating barbs on bio-inspired MNs, on the electric field, and surface area to understand their impact on acid/dye delivery. Anticipated outcomes suggest increased penetration depth of model drugs over time using bio-inspired MNs with ITP, indicating superior model drug delivery across gel. Detailed findings and comparative analyses elucidate differences in penetration depths between bio-inspired and cone MN configurations, providing insight into drug delivery efficiency. The study merges bio-inspired MNs with ITP for enhanced transdermal model drug delivery (TDD).

Using COMSOL Multiphysics 6.1, parameters like voltage distribution, electric field strength, and drug concentration within the skin are simulated. Bio-inspired MNs show superior electric field strengths, particularly at their edges, augmenting electrophoretic and diffusive flux, thereby improving drug concentrations within the skin. The maximum electric field strength measured is 50 V/m for cone MNs and significantly higher at 900 V/m for bio-inspired MNs, concentrated particularly at the edges of the bio-inspired MNs in contrast to the overall surface of cone MNs.

Length of created channels by cone MN is 1600 μm and by bio-inspired is 2400 μm. Moreover, the combined effect of cone MNs and ITP exhibits the deepest penetration, reaching ~2000 μm after 10 mins. The implementation of ITP as a driving force further amplifies the model drug's permeation through the punctured gel. Ultimately, bio-inspired microneedle array (MA) and ITP achieve a remarkable and synergistic enhancement in dye and acid delivery. The confluence of bio-inspired MA and ITP displays the deepest penetration depth, reaching ~2600 μm after 10 mins.

The diffusion of the model drug through microholes created by the cone MA significantly enhances permeation, reaching a depth of approximately 1000 μm, even without the application of ITP. Similarly, the bio-inspired MA-created microholes allow for model drug diffusion to deeper layers, enhancing permeation up to ~1400 μm without ITP after 10 mins. Higher fluorescence intensity, observed specifically in microholes created by the bio-inspired MA,

signifies a more extensive diffusion of the model drug solution into deeper gel layers facilitated by these microholes.

The investigation covers design, fabrication, experimental investigations, and discussions on outcomes and synergies between MNs and ITP. Examining varied MN geometries' impact on model drug permeation rates promises advancements in drug delivery methods.

**Keywords:** Microneedle, ITP, Drug Delivery Enhancement, Bio-inspired MNs, Microneedle Geometry, Transdermal Drug Delivery

# Table of Contents

# List of Figures

# List of Tables

## List of symbols and abbreviations

| | |
|---|---|
| MNs | Microneedles |
| TDD | Transdermal drug delivery |
| SC | Stratum corneum |
| ITP | Iontophoresis |
| SS | Stainless steel |
| SEM | Scanning electron microscopy |
| PuSL | Projection micro-stereo lithography |
| TENG | Triboelectric nanogenerator |
| EP | Electrophoresis |
| AC | Alternating current |
| FIEA | Flexible interdigitated electroporation array |
| RoMEA | Rolling MN electrode array |
| MCAO | Middle cerebral artery occlusion |
| SCS | Suprachoroidal space |
| IDPMAP | Iontophoresis-driven porous microneedle array patch |
| MMN | Mesoporous microneedles |
| rhGH | Recombinant human growth hormone |
| ICG | Indocyanine green |
| NMs | Nano-micelles |
| ZIF-8 | Zeolitic imidazolate framework-8 |
| PTT | Photothermal therapy |
| TMPH | Tetra-methylpyrazine hydrochloride |
| HA | Hyaluronic acid |
| TMAP | Transdermal microneedle array patch |
| STL | Stereolithography |
| FITC | Fluorescein Isothiocyanate |
| IMAP | Iontophoresis-MA-Patch |

## Acknowledgements

I want to thank Prof. Mina Hoorfar for her incredible guidance, helping me grow both in science and as a person. A big thank you to Nishat Tasnim, our previous lab manager, for making our lab a great place to work. I'm grateful to Somayeh Fardindoost for always being patient, kind, and supportive. Her help means a lot to me. Special thanks to Emily Earl and Jacob Stachowski for their valuable assistance in the lab. They've been a huge help.

And to all my lab mates and friends, thank you for being there, supporting me, and making this journey enjoyable both academically and emotionally.

Lastly, a heartfelt thanks to everyone else who supported and believed in me throughout this journey, even if their names aren't mentioned here.

## Dedication

To my wonderful parents and dear brothers,

Thank you for always being by my side. Even when we're far apart, your love and support reach me. You've given me strength and encouragement to chase my dreams. This thesis is dedicated to you, with all my love.

# Chapter 1: Introduction

## 1-1. MN-Based TDD

TDD, a method approved for clinical use since 1981, has revolutionized the administration of medications by enabling drugs to be delivered through the skin for the treatment of both local and systemic conditions [1]. This non-invasive approach to drug delivery boasts excellent bioavailability while bypassing issues such as gastrointestinal degradation and first-pass metabolism [2]. The human skin, with an expansive surface area exceeding 20,000 $cm^2$ in adults, offers a remarkable advantage for drug administration [3]. TDD has found extensive application in delivering macromolecules and vaccines like insulin, parathyroid hormone, and influenza vaccines. TDD is utilized for a wide spectrum of ailments, from cardiovascular diseases, Parkinson's, Alzheimer's, and various other medical conditions to anxiety disorders [4]. Nevertheless, a primary impediment to effective TDD is posed by the stratum corneum (SC), a 10-15 μm thick outermost layer of the skin consisting of dead corneocytes [5]. Various techniques, both active and passive, have been investigated to surmount this challenge. These encompass methods such as ITP, ultrasound, microwave, electroporation, thermal ablation, microneedles, as well as chemical enhancers and vehicle formulations [6].

Among the various approaches explored to enhance TDD, the MN delivery system has gained significant traction in recent years [1]. MNs, characterized by their minimal invasiveness, employ a base support and several MNs, each just a few microns in diameter. These MNs can be arranged singularly or in arrays numbering in the hundreds or thousands with lengths extending up to 2 mm and diameters spanning hundreds of microns. The versatility of MNs is reflected in the numerous materials they have been tested with, including silicon, ceramic, glass, metal, and polymers, as well as their diverse geometric configurations, including octagonal, cylindrical, rectangular, pyramidal, conical, and quadrangular [7]. The manufacturing techniques for MNs are equally diverse, involving methods such as etching, micro-molding, and lithography [8].

In the past three decades, extensive preclinical and clinical research data have been generated, enhancing the utility of the MN vaccine delivery system [1]. These micron-sized needles can transport molecules directly through the skin, cornea, the back of the eye, and the gut membrane, serving applications in medication administration, immunization, bio-sensing, and diagnostics [9][10][11]. A standout feature of MN delivery is its capacity for non-invasive, painless skin penetration, substantially enhancing patient safety and comfort. Moreover, MNs have demonstrated the ability to deliver a broad spectrum of substances, ranging from oligonucleotides, vaccines, antigens, virus-like particles, bioagents, proteins, insulin, human growth hormone, vitamins, small molecules, to macromolecules [7][8][9][10][11].

The diversity in MN designs has led to a wide range of drug delivery strategies. Solid, coated, hollow, dissolvable, and swellable MNs represent the five most common designs employed in MN drug delivery devices [11][12][13][14]. These various designs have distinct mechanisms of action. Solid MNs, for example, create transient micropores in the SC, enhancing the permeability of the barrier layer. Coated MNs were a pivotal advancement, pre-coating MNs with a vaccine in a formulation compatible with dissolution. Hollow MNs provide a pre-defined channel for drug administration, particularly for larger volumes of liquid formulations. Dissolvable MNs, on the other hand, are made from polymeric materials containing the drug, which dissolves upon insertion into the skin. Swellable MNs use a hydrogel structure that absorbs fluid from surrounding tissue, leading to the expansion of the needle core and the creation of channels through which therapeutic drugs can permeate (as seen in Figure 1) [11][12][13][14].

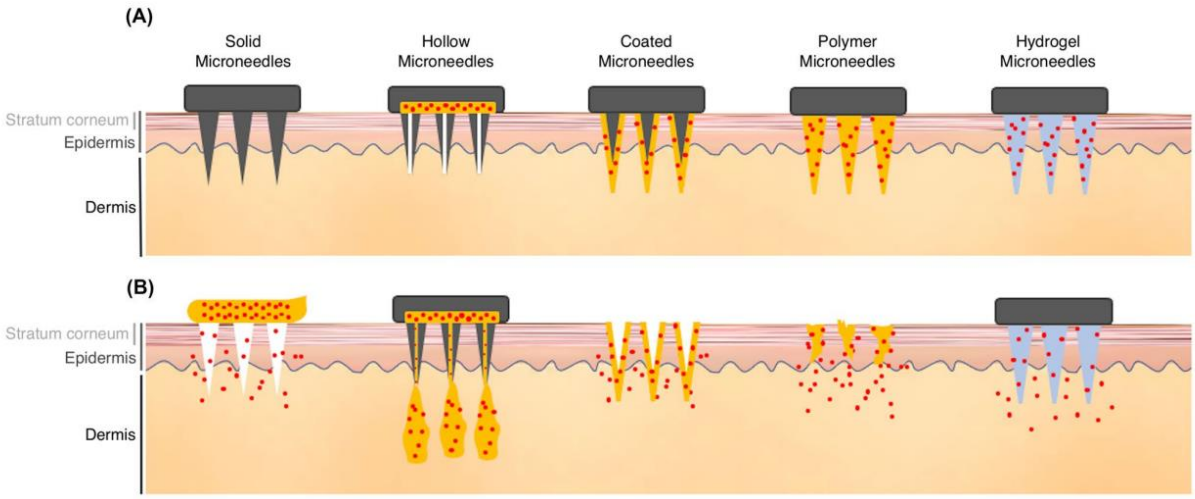


Figure 1. Types and characteristics of MNs for drug delivery. (A) Illustrations of solid, hollow, coated, polymer, and hydrogel MNs. (B) The drug delivery properties of these MNs differ. Solid MNs penetrate the skin and increase drug permeability. Hollow MNs create pathways for drug infusion. Coated MNs dissolve drug coatings on their surface after insertion into the skin. Polymer MNs, made with biocompatible and biodegradable materials, dissolve in the skin to release drugs. Hydrogel MNs made with non-dissolving, liquid-absorbing materials facilitate fluid and materials diffusion [12].

Furthermore, drug delivery employing MNs can be categorized into five distinct techniques. The 'poke and patch' strategy uses MNs, typically solid metal MNs, to create micropores in the skin, enabling the easier penetration of drug molecules administered to the treated area, whether as a solution, ointment, or transdermal patch [10]. The 'coat and poke' method entails using MNs pre-coated with the substance to be administered. These coated MNs are allowed to penetrate the skin, and they remain in place until the coating dissolves before being removed intact. The 'poke and release' approach relies on MNs composed of materials that can rapidly disintegrate and dissolve in interstitial fluid. Dissolving polymers or sugars are typically used in the creation of these MNs. Hollow-core MNs, which can carry larger volumes of liquids, have been employed for painless injections of liquid formulations into the body. The 'poke and swell' technique employs hydrogel-forming MNs that absorb interstitial fluid and swell [10].

Various methods have been developed to enhance skin permeability, including the use of permeation enhancers, which can be either chemical or physical. These enhancers have diverse modes of action, but their ultimate goal is to alter the structure of the SC, the primary barrier to substance absorption [15]. Chemical penetration enhancers have been developed and tested for

low molecular weight drugs to disrupt the barrier function of the SC [16]. However, for hydrophilic macromolecules like peptides, passive diffusion through the skin is not feasible.

To enhance the transdermal delivery of peptides and proteins, different approaches have been researched. Traditional permeation enhancers like fatty acids, alcohols, terpenes, and surfactants work by fluidizing or extracting SC intercellular lipids, opening tight junctions between keratinocytes, or increasing drug partitioning into the skin. However, their effectiveness is limited to small peptides. One method involves using cell-penetrating peptides conjugated to or co-administered with protein drugs. Other techniques, such as covalently or non-covalently linked protein transduction domains or nanocarriers, also aim to enhance macromolecule permeation [16].

To overcome the limitations of chemical enhancers, physical enhancement techniques have been investigated extensively [15]. These techniques employ mechanical, electrical, or acoustic forces to facilitate the movement of drugs through the skin, enhancing their absorption [17]. Some prominent methods include ultrasound, electroporation, thermal ablation, vibratory actuation, and magnetic fields [18][19][20][21]. Combining these physical enhancement techniques with MNs has shown great promise in improving drug delivery and control [22].

## 1-2. Combining MNs with Physical Techniques for Improved TDD

Numerous studies have investigated the combination of MNs with multiple physical enhancement methods to augment skin permeability. This section specifically explores the integration of MNs with techniques like electric field application, ultrasound, thermal ablation, vibratory actuation, and magnetic field application to enhance drug penetration through the skin in targeted application areas.

### 1-2-1. MN Geometry

While microfabrication technology-based MN arrays have shown promise in reducing voltage and damage in various studies, their practical use is limited due to the expensive and labor-intensive manufacturing process [23]. Modifying the MN surface allows for targeted medication

administration to a specific depth within the skin and facilitates increased drug loading. This can be achieved by coating the MNs successively with protective or secondary drug coats after their initial insertion into pockets, termed as "pocketed MNs" [24].

In a study, a cup-shaped solid stainless steel (SS) MN array was developed for regulated leak-proof medication delivery, using an out-of-plane configuration. The microcup structure of these MNs serves as a reservoir for medication, preventing leakage during skin insertion and enabling multi-drug delivery in optimal dosages [25]. For effective transdermal drug administration, the geometries and penetrating force of MNs are critical considerations. Injection-molded semi-hollow and bird-bill MN arrays are recommended for the transdermal delivery of high molecular-weight drugs, effectively creating micro-holes in the SC and allowing for mass production [26].

The creation of cone-shaped MN arrays with microchannels embedded within the MNs demonstrates exceptional drug delivery potential (see Figure 2). Known as a multi-microchannel MN microporation (4M) platform, it facilitates high-efficiency intracellular distribution in vivo, offering safety, uniformity, and enhanced efficacy. Internal microchannels formed through precise 3D printing provide a concentrated, safe electric field. This not only expedites cargo movement into deep tissue during electrophoresis but also triggers cell electroporation, improving transport across cell membranes. This methodology holds promise for developing new medications, particularly for solid tumor treatment [27].

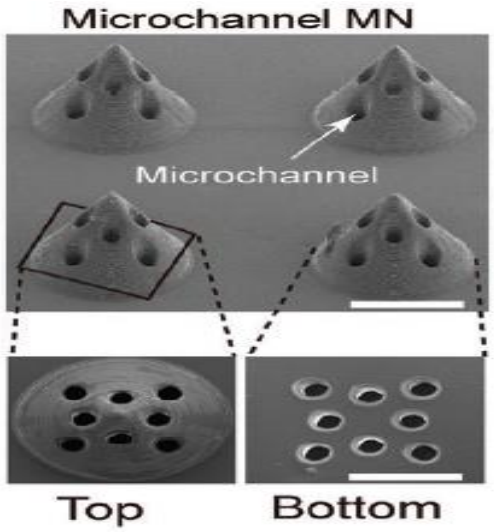


Figure 2. Scanning electron microscopy (SEM) images of the MNs with built-in microchannels, enhancing drug delivery for solid tumor treatment via cone-shaped MN array and internal microchannels (Scale bar, 200 μm) [27]

Moreover, grooved MNs, capable of accommodating higher drug loads, represent an avenue for enhanced drug delivery. A patch-type MN platform has been proposed to deliver various liquid medications and vaccines into the skin rapidly, requiring only gentle pressure with the thumb against the skin. Inspired by snakes' teeth, this approach bypasses the need for complex pumping mechanisms or drug reformulation. Liquid delivery in this scenario relies on surface tension and capillary action as fundamental mechanisms [28].

Advancements have been taken in developing bio-inspired MNs, inspired by natural models like mosquito mouthparts. The initial work involved creating a hollow silicon MN, mimicking the mosquito's proboscis. Experimentation and simulations were utilized to understand fracture features and insertion forces. Progress extended to crafting jagged MNs from biodegradable polymer, significantly reducing insertion force through vibration inspired by mosquito behavior. Utilizing high-frequency vibrations reduced insertion force in hollow MNs due to dynamic stiffness, cavitation, and localized thermal damage [29]. Remarkable advancements include lancets featuring micro-sawteeth and hypodermic needles with irregular surfaces, underscoring the profound impact of microstructures [30][31].

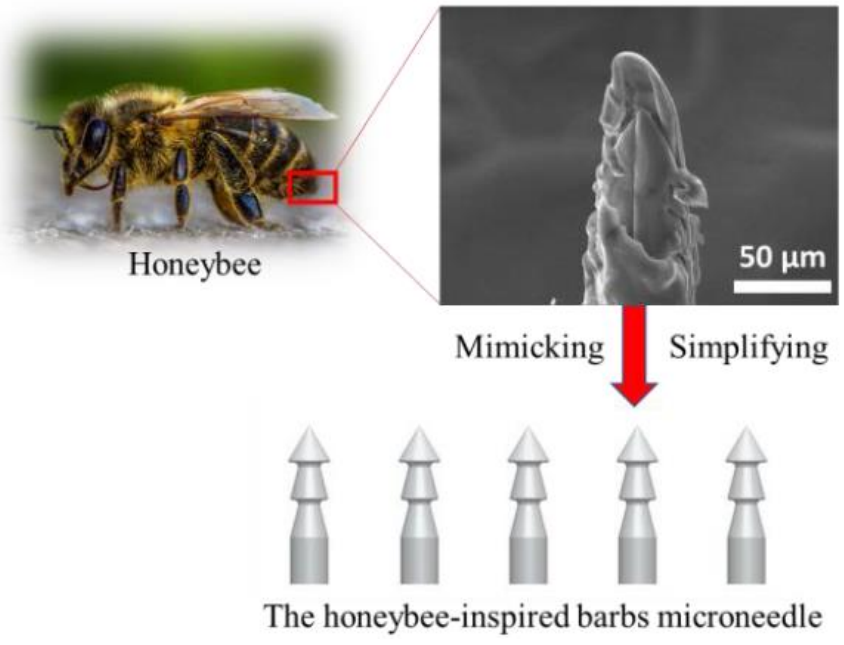


Figure 3: Schematic design of a barbed MN inspired by the honeybee stinger, engineered for easy skin penetration and secure interlocking. [32]

Efficient tissue adhesion often draws inspiration from nature's ingenious designs, such as the honeybee stinger—a simple yet effective model. The stinger, developed for single-use purposes, consists of barbs along two stylets, enabling easy skin penetration and challenging removal (as shown in Figure 3). Researchers have endeavored to replicate this mechanism. Their MN design with micro-barbs mimics the honeybee stinger, reducing insertion force and enhancing adhesion during retraction. This micro-barbed MN showed a triple increase in the retraction-penetration force ratio compared to barbless ones. Medical applications require non-irritating, non-toxic adhesives to ensure safety when penetrating deeply into the skin. Therefore, utilizing biocompatible and biofunctional materials like biodegradable silk fibroin in MNs becomes crucial due to their mechanical strength, low degradation rate, and biocompatibility [33, 34,35].

The biomedical field faces challenges in establishing durable tissue adhesion, especially in diabetes care with the need for frequent hypodermic needle injections. MNs offer potential solutions. A recent study introduced a polymeric adhesive tape with mushroom-like micropillars, albeit with about 47% adhesion strength compared to chemical adhesives [36]. Seeking solutions, inspiration was drawn from nature: the mosquito's proboscis, honeybee stinger, and porcupine quills exhibit remarkable insertion and adhesion mechanisms. Bio-inspired MNs have shown promise; biphasic MNs with swelling tips, inspired by an endoparasite, ensured minimal penetration force and robust adhesion [37]. Similarly, replication of porcupine quill barbs facilitated easy penetration and strong adhesion [38]. Challenges persist in fabrication complexity and the need for improved tissue adhesion. To address this, 3D MNs with backward-facing curved fins, akin to porcupine quills or honeybee stingers, were fabricated using projection micro-stereo lithography (PuSL). This bio-inspired MN holds promise for applications in TDD and biosensing [39].

### 1-2-2. MNs Combined with Electric field

ITP and electroporation methods leverage electric fields to enhance the dispersion of topical and transdermal medications [40]. Skin electroporation involves brief electrical pulses that modify skin permeability by creating an aqueous pathway in the stratum SC, facilitating improved drug delivery through an electrical driving force [41]. Iontophoretic transdermal patch (ITP) application

uses a low-level electric current to push medication through the skin. While ITP primarily influences the drug itself, electroporation affects the skin and, during a pulse, interacts with the drug [42]. While ITP application has shown efficacy in delivering small therapeutic molecules, transporting larger macromolecules like proteins encounters challenges due to the SC barrier, prompting exploration of alternative methods [43].

Moreover, the MNs are specifically designed at 650 μm in length, concentrating the electric field in the epidermis, known for its abundance of antigen-presenting cells. This design aims to avoid stimulating sensory and motor nerves deeper in the dermis or muscular tissues [44]. The combination of MNs and ITPs appears to enhance transdermal medication delivery [45]. Additionally, employing MNs in conjunction with electroporation can augment SC permeability, enhancing transdermal drug release systems to accommodate macromolecules up to 40 kDa. This approach minimizes the need for specific permeation-enhancing agents, thereby reducing the likelihood of associated irritating adverse effects [46].

#### 1-2-2-1. MNs Combined with Electroporation

Combining MNs with electroporation mitigates potential issues arising from the use of conventional devices due to large electrode size and high voltage, reducing risks of physical damage and electric burns [47]. In this approach, electrically conductive MN electrodes form arrays that puncture the outer skin layer, establishing direct contact with the highly conductive epidermis beneath, bypassing the high-impedance SC and enhancing the electric field within the tissue. MNs also concentrate a stronger electric field at their tips, potentially enhancing their efficacy. Additionally, MN lengths can be adjusted to prevent nerve stimulation, ensuring painless application [44],[48].

Portable medication delivery systems incorporating MNs and a triboelectric nanogenerator (TENG) have been proposed to overcome portability limitations in electroporation. The TENG replaces the electrophoresis (EP) effect, converting mechanical energy into alternating current (AC) as a self-powered system. It boasts simplicity, cost-effectiveness, and high output performance over other self-powered devices [49].

While electroporation holds wide applications, the high cost of electroporators restricts access for many budget-constrained laboratories. To address this, a cost-effective, portable electroporator was developed using a household piezoelectric stove lighter. This device generates repeatable,

effective pulses for cell electroporation, presenting a viable alternative to expensive electroporation setups. An ultra-low-cost, portable electroporation device (<1 USD, <50 g), called "ePatch," is reported for DNA vaccination against SARS-CoV-2 [44].

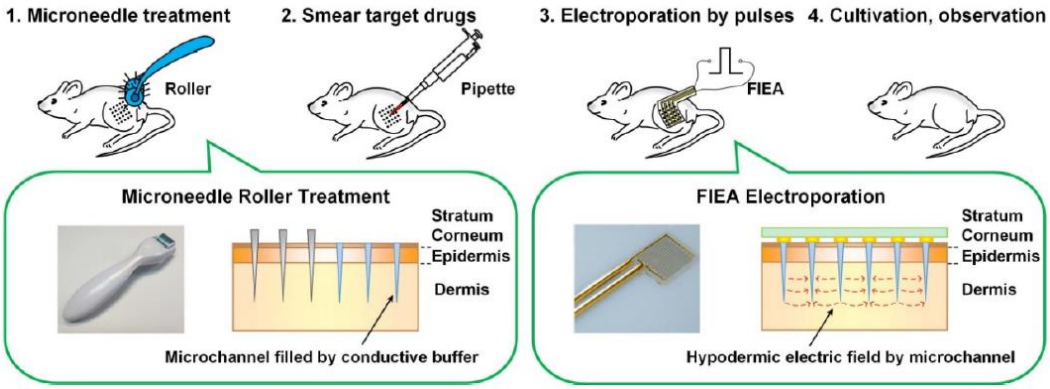


Figure 4: A pioneering electroporation technique utilizing a MN roller alongside a flexible interdigitated electroporation array (FIEA) [41].

The effective delivery of nucleic acids across diverse tissue structures poses a challenge due to irregular tissue shapes, particularly in tissues such as the skin. To address this, a cost-effective, minimally invasive in vivo electroporation technique combines a flexible electrode and a MN roller (shown in Figure 4). This approach enhances drug delivery efficiency using low voltage by creating paths through the skin's outer layer (SC) via the MN roller.

Comparatively, the flexible electroporation array maintains close contact with the targeted surface, generating a uniform electric field with a low voltage (50 V). This technique ensures effective delivery without skin or muscle damage in treated subjects, improving transfection rates and minimizing skin injury compared to conventional methods [41],[23].

Efforts are underway to streamline the procedure further, boost efficiency, and explore potential clinical applications. A rolling MN electrode array (RoMEA) is an efficient and less invasive siRNA delivery tool that uses parallel circular blade electrodes embedded with MN arrays. RoMEA creates uniform micropores, enabling effective siRNA administration and gene silencing across tissues. Its non-invasive, cost-effective, and mass-producible design holds promise for various applications, including cancer immunotherapy, enhancing its potential for clinical use [47].

### 1-2-2-2. Combining MNs with ITP

Combining MNs with ITP presents a promising drug delivery strategy [41]. ITP, employing continuous or pulse current flow, drives ions through the skin, offering targeted therapy for various conditions like eye diseases, oral ailments, and cancer [41], [50], [51]. To overcome macromolecule delivery limitations, MNs combined with ITP are under investigation, showing enhanced efficiency in diverse medication delivery routes [41].

This innovative approach exhibits potential in managing obesity via transdermal metformin delivery [52]. MN-assisted transdermal delivery aims to mitigate obesity while reducing gastrointestinal side effects [52]. Furthermore, this method showcases promise in conditions like psoriasis, where altered skin features affect drug permeation and retention [53]. In neurological conditions such as middle cerebral artery occlusion, the combined MN-ITP approach reduces infarct volumes and enhances drug distribution in the brain [45].

Regarding ocular medicine delivery, ITP combined with MNs targets the posterior eye more effectively, boosting nanoparticle delivery to the most posterior region of the suprachoroidal space (SCS) in the rabbit eye (as seen in Figure 5) [54]. This innovative approach demonstrates potential for targeted ocular drug delivery.

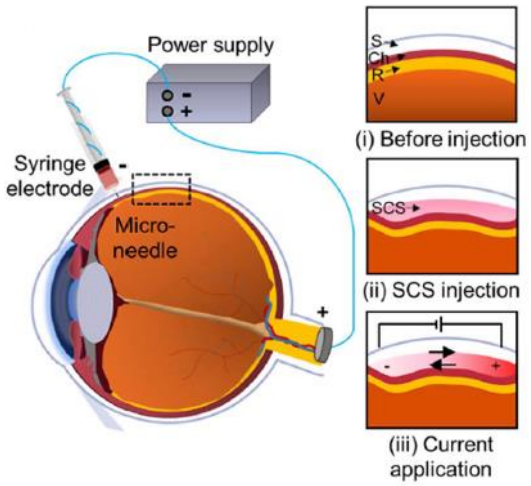


Figure 5: Schematic of iontophoretic targeting for delivering ocular medicine via the SCS. (i) the gap between the sclera and choroid, (ii) the filling of the SCS with the injected medicine formulation, and (iii) the use of ITP to propel charged species within the SCS [54].

The use of MNs combined with ITP has been explored for various molecules, including small molecules, peptides, and proteins, to assess potential synergies due to their different operating mechanisms and outcomes [55]. Transdermal administration of baclofen utilizes a combination of ITP and MN methods, demonstrated in Figure 6, due to its hydrophilic nature, necessitating this dual approach to achieve effective therapeutic levels [56]

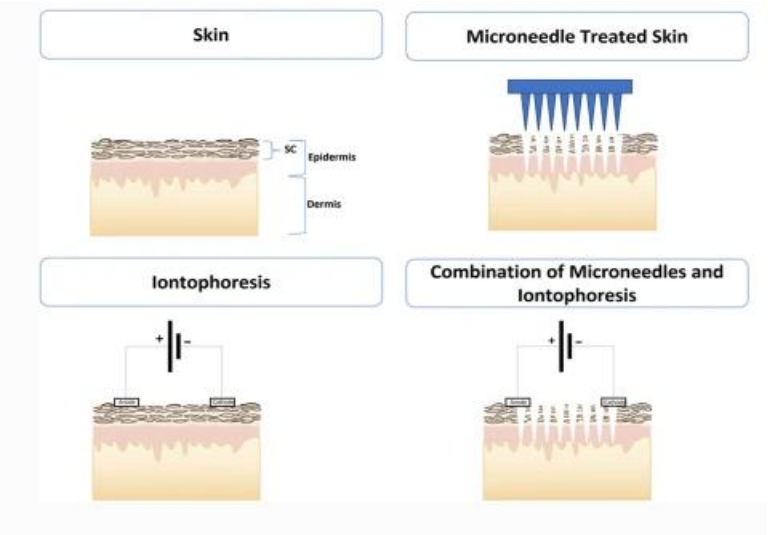


Figure 6: Transdermal administration of baclofen through the combination of ITP and MNs [56].

The combination of porous MNs with ITP for TDD is challenging due to complex manufacturing and fragility. A novel approach introduced an ITP-driven porous MN array patch (IDPMAP), enhancing drug delivery efficiency and control [57]. These MNs significantly decreased skin resistance, allowing the formation of transdermal electrical fields, while mesoporous MNs (MMN) facilitated painless skin penetration for glucose extraction and insulin administration [58],[59]. Dissolving MN systems with ITP demonstrated enhanced skin penetration of sumatriptan succinate [60]. The permeation-enhancing effects of iontophoretic delivery via microchannels were evaluated for transdermal administration of recombinant human growth hormone (rhGH) (as seen in Figure 7) [61]. Another innovation, the ITP-driven MN array patch (IMAP), combines solid MNs and ITP, showing potential for enhanced treatment of type 1 diabetes [43].

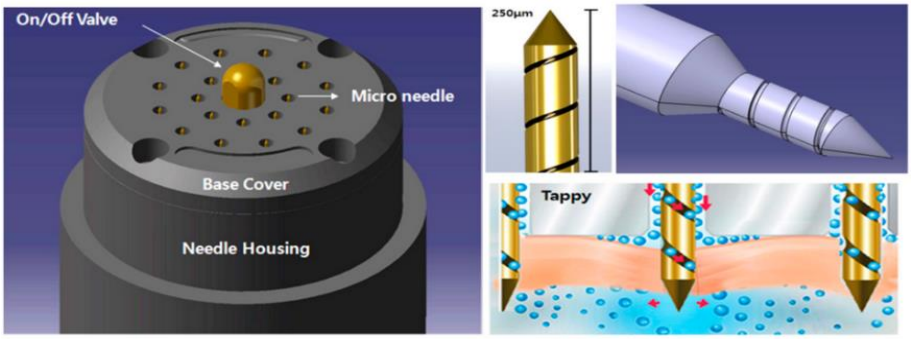


Figure 7: Schematic diagram of the Tappy Tok Tok® MN device for transdermal rhGH delivery via ITP through microchannels [61].

### 1-2-3. MNs Combined with Ultrasound

Studies have explored the synergy between ultrasound and MNs to enhance drug permeability through the skin [62-64]. This combination has proven effective for increasing the delivery of hydrophobic compounds like zidovudine (AZT) and lidocaine [65-67], along with facilitating the transdermal delivery of biomacromolecules such as siRNA and ovalbumin [67]. Mechanisms underlying this enhanced permeability include mechanical effects, heat, and cavitation generation within the skin [66]. Techniques like bubble-generating MNs have been proposed to augment drug penetration in various tissues, including keloid scars and tumors [68-71].

AZT, an antiviral drug for HIV-1, faces limited permeability through healthy pigskin. However, sonophoresis treatment significantly improved its permeability, reducing the lag time for drug absorption [65]. Lidocaine, a water-soluble acid administered via hypodermic needles, was explored for improved epidermal delivery using MNs and ultrasound. Ultrasonic pre-treatment increased lidocaine permeability, requiring less time to reach therapeutic levels. Higher low-frequency ultrasound power exhibited a more significant impact than increased exposure time [66].

Treatment of keloid lesions (pathological scars) traditionally involves steroids administered through hypodermic injections, which can cause discomfort. MNs alone could not effectively deliver medication deep into the scar, but combining them with ultrasound after implanting a polylactic acid MN array showed promise in controlling keloid growth in preclinical and clinical trials [70]. This approach demonstrated effectiveness in delivering triamcinolone on both normal and keloid skin.

Studies exploring TDD are investigating bubble-generating MNs under ultrasound. These MNs create micro/nanobubbles via electrolysis or chemical reactions [68-69], [71–72]. Loading micro/nanobubbles into MNs has demonstrated improved intradermal drug delivery depth while reducing required ultrasonic power.

One innovative approach proposed fabricating nanobubble-based MN layers to release drugs with ultrasound. This method involved coating Poly (lactide-co-glycolic acid) PLGA MNs with polylysine to create a positive charge surface, then adsorbing negatively charged drug-containing nanobubbles. Ultrasound triggered the liposome-encapsulated perfluoro hexane nanobubbles to generate bubbles (as shown in Figure 8) [69].

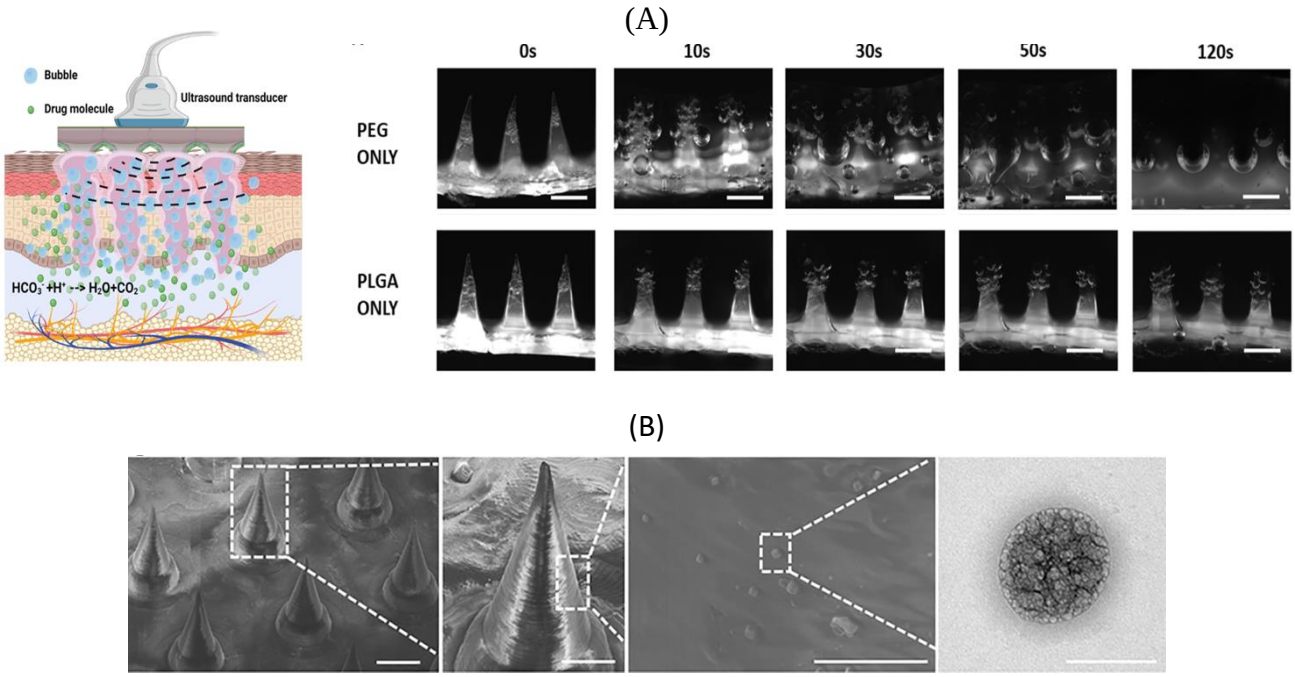


Figure 8: A) The combination of active MNs and ultrasound. Following MN insertion into the skin, interstitial fluid diffused into the MN's polymeric matrix, resulting in the production of bubbles via citric acid and NaHCO3 [68]. B) A scanning electron microscope (SEM) image showing lipid nanobubbles formed on the MN surface [69]

### 1-2-4. MNs Combined with Thermal Ablation

Research has investigated combined photothermal and chemotherapy treatments using drug-loaded MNs, including various nanomaterials like $CuO_2$ nanoparticles [73], IR780 [74], [75], lanthanum hexaboride [73], and Prussian blue nanocubes [76]. These MNs aim to spatially control

drug administration, allowing on-off release patterns with improved biosafety and light-activated heating for multiple cycles.

$CuO_2$ nanoparticles in poly(vinylpyrrolidone) (PVP) MNs reacted under tumor acidity, releasing $Cu^{2+}$ and hydrogen peroxide to induce cellular oxidative damage via $^{\bullet}OH$ generation [77]. Gelatin/sucrose film-coated MNs efficiently delivered molecules like bovine serum albumin, doxorubicin, and indocyanine green (ICG), demonstrating time-dependent photothermal effects [78]. IR780-loaded nano-micelles (NMs) co-delivered paclitaxel (PTX) and IR-780 to skin tumors, showing significant tumor growth inhibition [74]. Polycaprolactone (PCL) MNs loaded with photothermal agents like lanthanum hexaboride and Prussian blue nanocubes delivered doxorubicin (DOX) (figure 9) [73], [76]. These MNs melted under near-infrared (NIR), releasing DOX into tumors. AuNC-loaded MNs exhibited promising tumor growth inhibition in mouse models [79]. AuNCs enhanced MN mechanical strength and photothermal effects, allowing lower mass concentration for similar therapeutic effects. CuS nanoparticles were integrated into zeolitic imidazolate framework-8 (ZIF-8) to improve camptothecin distribution in tumors [80]. While chemotherapy showed better melanoma inhibition in vivo, a synergistic effect arose when combined with photothermal therapy (PTT), attributed to reduced tumor cell growth and apoptosis [80]. Introducing α-tocopheryl succinate (TPGS) into poly (lactic-*co*-glycolic acid) nanoparticles (PLGA NPs) enhanced drug release and hydrophilicity, addressing limitations in circulation time, cell attachment, and hydrophobic drug delivery, thereby improving melanoma treatment via dissolving MNs [81],[82].

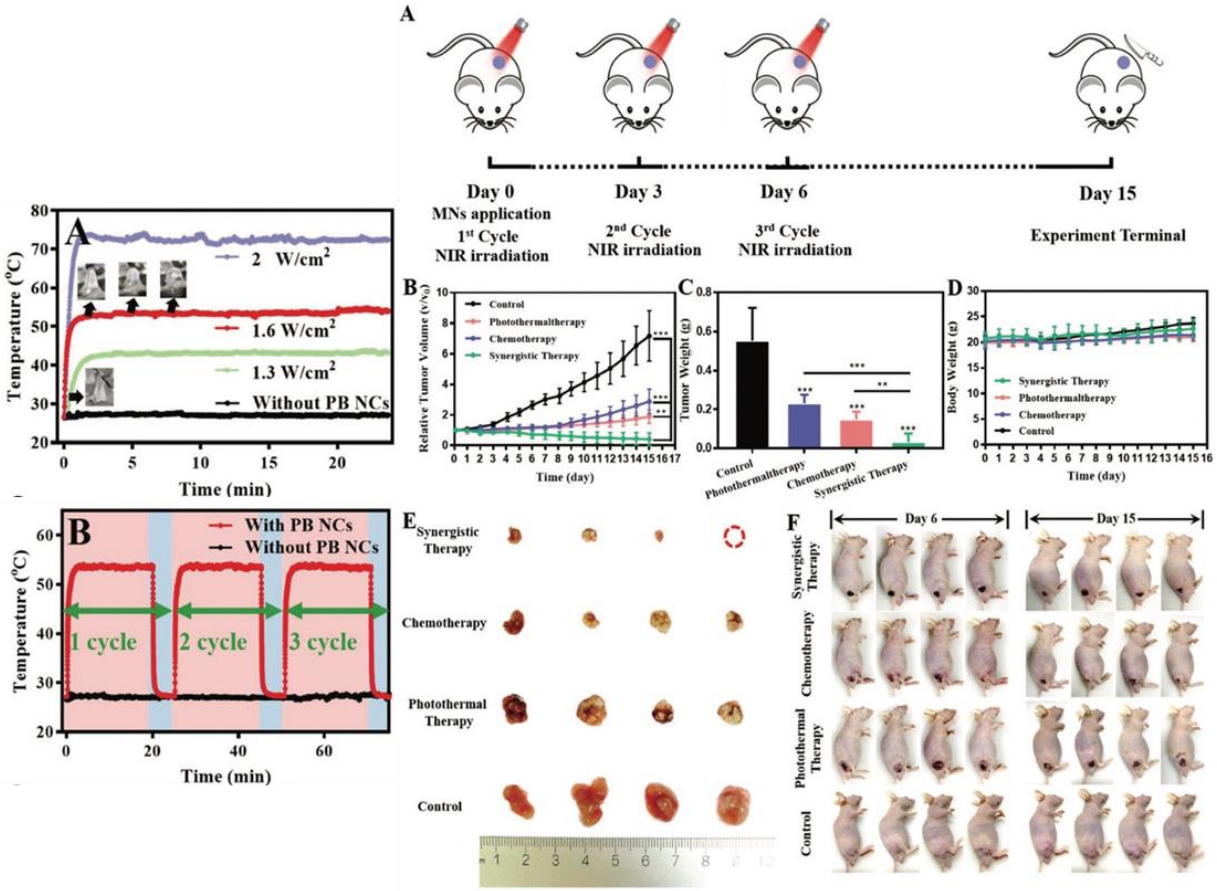


Figure 9: Utilizing dissolving MNs to enhance cancer therapy by combining chemotherapy with photothermal therapy (PTT) [76]

### 1-2-5. MNs Combined with Vibratory Actuation

Numerous investigations explored mechano-physical stimuli like vibration to enhance TDD, drawing inspiration from mosquito skin-piercing techniques [83-86]. The role of stretch and mechanical vibration on skin resistance was studied, affecting puncture depth and force, revealing that stretching aided deeper and more precise MN penetration [87]. Finite element simulations illustrated that vibration during MN insertion reduced stress, facilitating the creation of deeper and larger microchannels with less deformation [88]. In vivo studies demonstrated improved insulin and tetra-methylpyrazine hydrochloride transdermal delivery with increasing vibration frequency [89]. Assessments on vitamin C permeation highlighted increased penetration depth with higher application power and intensity [90].

### 1-2-6. MNs Combined with Magnetic Field

Researchers have explored magnetically-controlled MNs for drug delivery, utilizing methods like hollow MN systems with battery-free magnetic pumps, MN robots for oral drug delivery, and modified multilayer MN patches within magnetically-actuated capsules [91-94]. These innovations aim to deliver drugs through dissolving, create channels in the skin, and enhance adhesion and protection in the gastrointestinal system. The battery-free device showed controlled drug release ex vivo, but further in vivo studies considering variables like skin thickness and movement are necessary (as seen in Figure 10) [91]. MN robots for oral drug delivery demonstrated practical potential in ex vivo and in vivo trials, particularly for delivering insulin to minipigs [92]. Meanwhile, modifications in multi-layer MN patches within capsules were proposed to penetrate intestinal lesions, but further animal studies are needed to validate practical use due to insufficient adhesion and exposure to intestinal fluids [93-94].

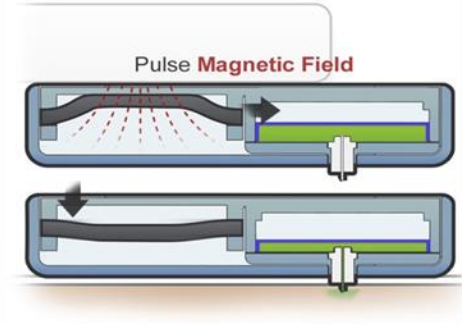


Figure 10: various applications using MNs and magnetic fields: Magnetic volume displacement pump driven by a magnetic field [91].

### 1-2-7. MNs Combined with Multiple Physical Methods

A novel drug delivery system integrates dissolving hyaluronic acid (HA) MN patches with ultrasound and ITP, demonstrating enhanced drug permeation and reduced initial delivery time compared to passive methods or ultrasonication. In vitro experiments validate that the combination of ultrasonic waves and ITP within MNs augments delivery efficiency and minimizes drug administration duration. This technology holds promise for the delivery of macromolecules and various medications, potentially transforming drug delivery processes, thus enhancing patient

outcomes and life quality. Further advancements could extend its applicability across a wide spectrum of drugs, facilitating more efficient and targeted medication delivery. Overall, this proposed system presents encouraging results, signifying a potential breakthrough in drug delivery approaches [95].

## 1-3. Motivation and Objectives

This experimental study aims to explore the potential enhancements in model drug delivery by combining MN technology with ITP, particularly focusing on the transition from conventional cone-shaped MNs to bio-inspired MNs. The primary objective is to assess how this alteration in MN geometry, featuring barbs on the bio-inspired MNs, can augment the electric field, surface area, and volume, potentially affecting the microholes created within the delivery matrix.

The anticipated outcomes involve an increased penetration depth of the model drug over time using bio-inspired MNs combined with ITP, signifying potentially superior model drug delivery across skin model barriers. The study aims to comprehensively present detailed findings and comparative analyses to elucidate variations in penetration depths between bio-inspired and cone MN configurations, facilitating a deeper understanding of their impact on drug delivery efficacy.

## 1-4. Thesis Outline

The thesis aims to combine bio-inspired MNs with ITP for enhanced TDD. Utilizing COMSOL Multiphysics 6.1, key parameters including voltage distribution, electric field strength, and drug concentration within the skin were simulated and analyzed. Bio-inspired MNs exhibited superior electric field strengths, particularly at their edges, augmenting electrophoretic and diffusive flux. The 'poke and patch' method was used, inserting MNs into the skin to transfer drugs consistently across skin thickness. We validated outcomes by replicating previous conditions and modifying MN geometry. Notably, geometries with five edges and an applied electrical current outperformed traditional cone-shaped MNs, leading to superior drug concentrations within the skin. The experimental study focuses on evaluating the efficacy of bio-inspired MNs with ITP for enhanced dye delivery. It explores alterations in MN geometry and delves into detailed investigations encompassing skin anatomy, model creation, and charged particle movement under an electric field. The outcomes will analyze the synergy between MNs and ITP, assessing varying MN configurations on model drug permeation rates and the mechanisms governing dye delivery.

# Chapter 2: Numerical Study on MN Optimization and Integration

Our study aimed to synergize bio-inspired MNs with ITP to enhance TDD. Using COMSOL Multiphysics 6.1, we meticulously simulated and analyzed vital parameters—voltage distribution, electric field strength, electrophoretic flux, and drug concentration within the skin. Employing the 'poke and patch' method, MNs were inserted into the skin to transfer drugs, maintaining consistent conditions of current across skin thickness. To bolster confidence in our outcomes, we replicated previous study conditions and modified MN geometry to understand its impact on outcomes. Initial validation of our findings involved a comparative analysis with relevant literature. Subsequent fine-tuning of MN geometries, notably those with five edges along with an applied electrical current, outperformed traditional cone-shaped MNs, leading to superior drug concentrations within the skin model. This highlights the potential efficacy of bio-inspired MNs coupled with ITP, providing an efficient and painless method for TDD, overcoming the skin's barrier effectively.

## 2-1. Comparative Analysis of Electric Field and Drug Delivery Efficiency between Cone and Bio-Inspired MNs

The computational investigation utilized the COMSOL Multiphysics 6.1 platform to examine the release of charged species, focusing on concentration and electrophoretic flux magnitude. The simulation framework centered on the Electric Currents and Transport of Diluted Species physics modules. By employing Fick's first law of diffusion, the model calculated the steady-state flux (Jss) of drug diffusion through the skin, represented as Jss = -D $\frac{dC}{dx}$. Here, 'D' signifies the drug's diffusion coefficient, 'C' stands for concentration, and 'dC/dx' depicts the concentration gradient. The simulation considered various materials, including skin, air microchannels formed by MNs, and hydrochloric acid (HCL) as a drug model, with an initial skin concentration of 0 mol/$m^3$. The simulation also assumed complete contact between the MN surface area and the skin upon insertion, adopting the 'poke and patch' technique for delivery.

Our configuration included the formation of microchannels in the skin. To achieve this, we utilized both conventional cone-shaped MNs and bio-inspired MNs featuring five edges. We opted

for HCl, a charged species, as our model drug to assess the performance of these microchannels in drug delivery. To maintain consistent conditions, we aimed to achieve a 3 mA-current through 1 mm thick skin. Initially, an electric potential is established between the MN array and the skin to ascertain the pronounced influence of MN geometry on electric field distribution and electrophoretic flux magnitude. To conduct a comprehensive investigation, two distinct geometrical configurations are taken into account: cone MNs and bio-inspired MNs. As depicted in Figure 11, the application of electric potential is discernible across the two distinct geometric configurations: cone MNs and bio-inspired MNs. Table 1 presents a comprehensive compilation of the geometric parameters utilized across all simulations detailed within this section.

(a) (b)

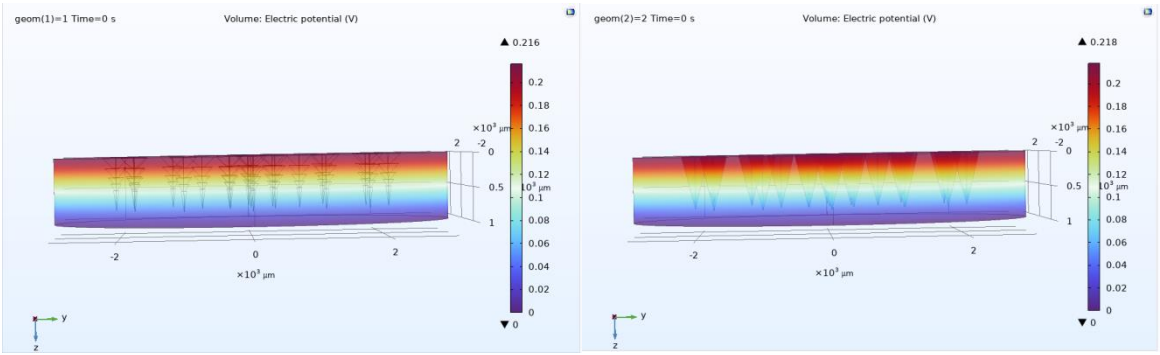


Figure 11: The simulation of electric potential with (a) bio-inspired and (b) cone MNs

Table 1: Geometry parameters

| **Name** | Expression | Description |
|---|---|---|
| *BR* | *200* µm | *Bottom radius of first edge on a bio-inspired MN* |
| *BR1* | *160* µm | *Bottom radius of second edge on a bio-inspired MN* |
| *BR2* | *120* µm | *Bottom radius of third edge on a bio-inspired MN* |
| *BR3* | *80* µm | *Bottom radius of fourth edge on a bio-inspired MN* |

| | | |
|---|---|---|
| *BR4* | *40* µm | *Bottom radius of fifth edge on a bio-inspired MN* |
| *H* | *160* µm | *Height of first edge on a bio-inspired MN* |
| *H1* | *140* µm | *Height of second edge on a bio-inspired MN* |
| *H2* | *100* µm | *Height of third edge on a bio-inspired MN* |
| *H3* | *100* µm | *Height of fourth edge on a bio-inspired MN* |
| *H4* | *300* µm | *Height of fifth edge on a bio-inspired MN* |
| *TR* | *40* µm | *Top radius of first edge on a bio-inspired MN* |
| *TR1* | *35* µm | *Top radius of second edge on a bio-inspired MN* |
| *TR2* | *30* µm | *Top radius of third edge on a bio-inspired MN* |
| *TR3* | *15* µm | *Top radius of fourth edge on a bio-inspired MN* |
| *TR4* | *0* µm | *Top radius of fifth edge on a bio-inspired MN* |
| *Current* | *3 mA* | *Current across skin with 1mm thickness* |
| *Height_cone* | *800* µm | *Height of cone MN* |
| *BR* | *200* µm | *Bottom radius of cone MN* |

Bio-inspired MNs exhibit distinct edges that contribute to the creation of higher electric field intensities. These edges facilitate the concentration of electric field lines, resulting in an elevated electric field magnitude throughout the MN structure. Due to their intricate design, bio-inspired MNs provide a more distributed and intensified electric field profile across their surface. This amplified electric field is especially prominent at the edges, resulting in enhanced particle interactions and field-driven effects, which can be advantageous for applications involving ITP and drug delivery. Cone MNs also possess edges; however, the electric field distribution around these edges might not be as concentrated as in bio-inspired MNs. Consequently, cone MNs may

offer a less pronounced electric field effect at their edges, impacting particle movement and interactions to a comparatively lower extent. The maximum electric field strength measured is 50 $\frac{V}{m}$ for cone MNs and significantly higher at 900 $\frac{V}{m}$ for bio-inspired MNs, concentrated particularly at the edges of the bio-inspired MNs in contrast to the overall surface of cone MNs. Figure 12 shows the simulation of electric field with bio-inspired and cone MNs.

(a) (b)

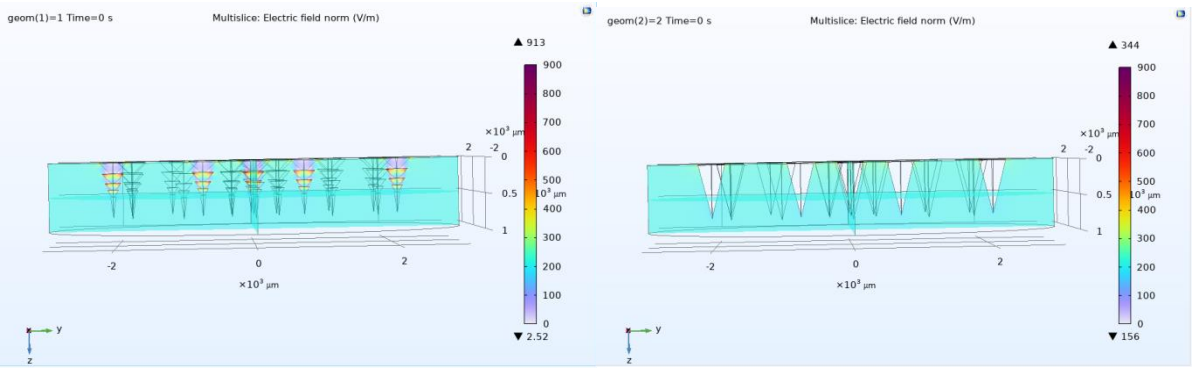


Figure 12: The simulation of electric field with (a) bio-inspired and (b) cone MNs

Higher electric field magnitude, as anticipated in bio-inspired MNs, can indeed lead to higher electrophoretic flux magnitudes (Table 2). The intensified electric field can accelerate charged particle movement, resulting in a more pronounced electrophoretic effect (figure 13). Cone MNs, while also contributing to electrophoretic movement, may not achieve the same level of flux magnitude as bio-inspired MNs due to their potentially lower electric field intensity.

(a) (b)

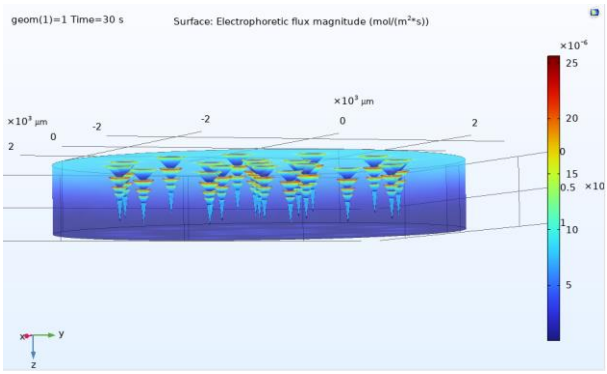
geom(1)=1 Time=30 s
Surface: Electrophoretic flux magnitude (mol/(m²*s))

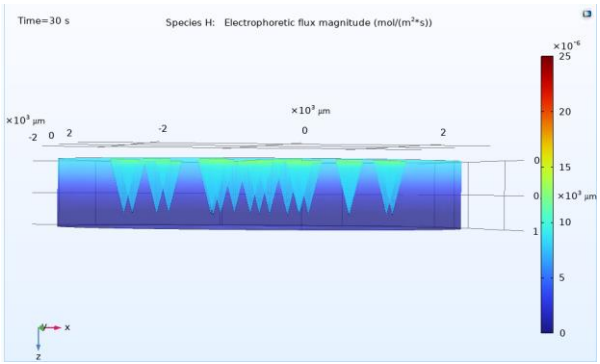
Time=30 s
Species H: Electrophoretic flux magnitude (mol/(m²*s))

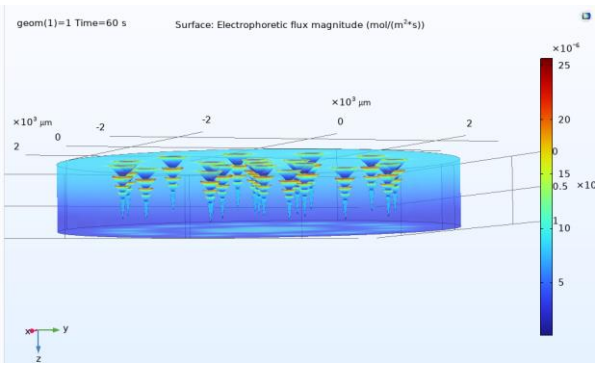
geom(1)=1 Time=60 s
Surface: Electrophoretic flux magnitude (mol/(m²*s))

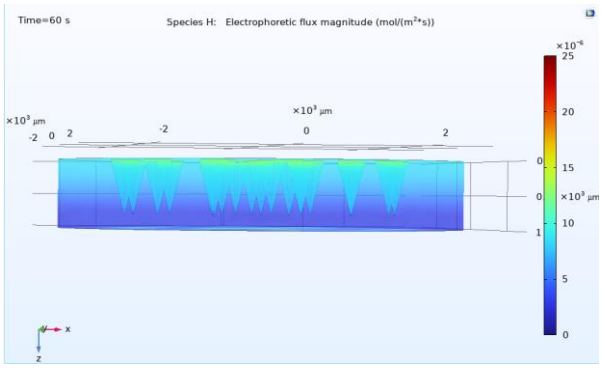
Time=60 s
Species H: Electrophoretic flux magnitude (mol/(m²*s))

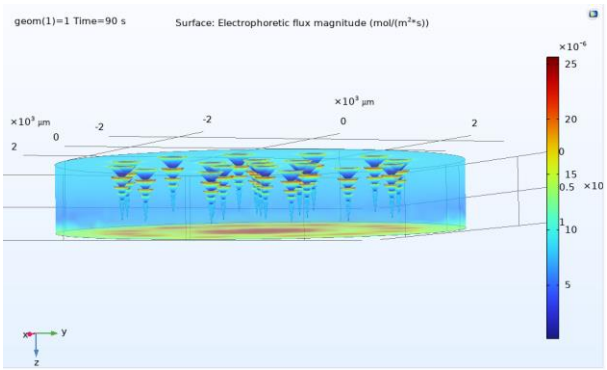
geom(1)=1 Time=90 s
Surface: Electrophoretic flux magnitude (mol/(m²*s))

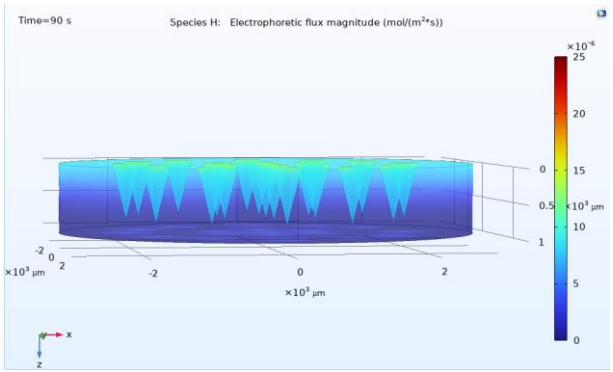
Time=90 s
Species H: Electrophoretic flux magnitude (mol/(m²*s))

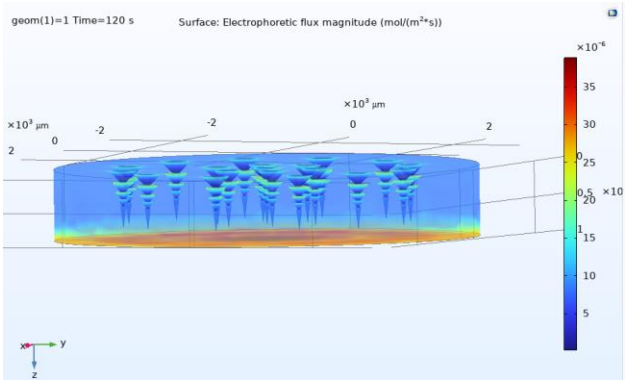
geom(1)=1 Time=120 s
Surface: Electrophoretic flux magnitude (mol/(m²*s))

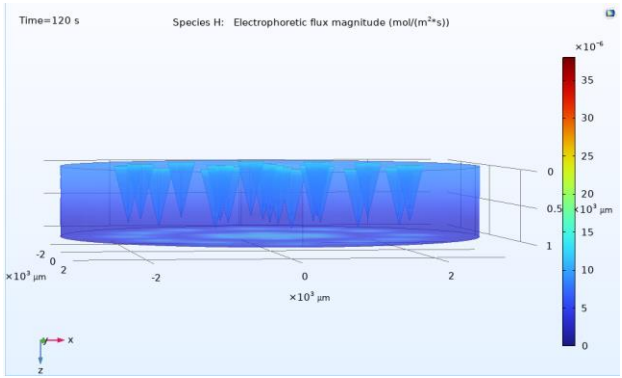
Time=120 s
Species H: Electrophoretic flux magnitude (mol/(m²*s))

Figure 13: Comparison of electrophoretic flux magnitude simulated over varied time frames (30 s, 60 s, 90 s, 120 s) between (a) bio-inspired and (b) cone MNs.

Bio-inspired MNs, with their higher surface area resulting from intricate features, could indeed exhibit higher diffusive flux magnitudes. The increased surface area enhances the chances of particle interaction and diffusion. Cone MNs, while contributing to diffusive flux, might not match the enhanced surface area of bio-inspired MNs, potentially resulting in comparatively lower diffusive flux magnitudes.

After 120 seconds, a notable 3-fold increase in charged species concentration is evident on the opposing side of the 1 mm-thick skin when employing bio-inspired MNs (figure 14). This observation unequivocally establishes the enhanced performance of bio-inspired MNs in terms of charged species concentration. Specifically, after 120 seconds, the concentration reaches an impressive 4.5 $mol/m^3$ on the opposite side of the skin. This region corresponds to the application site where the electric potential is applied, with a 1 mm separation between the positive and negative terminals. Consequently, bio-inspired MNs emerge as a favorable choice for ITP applications.

(a) (b)

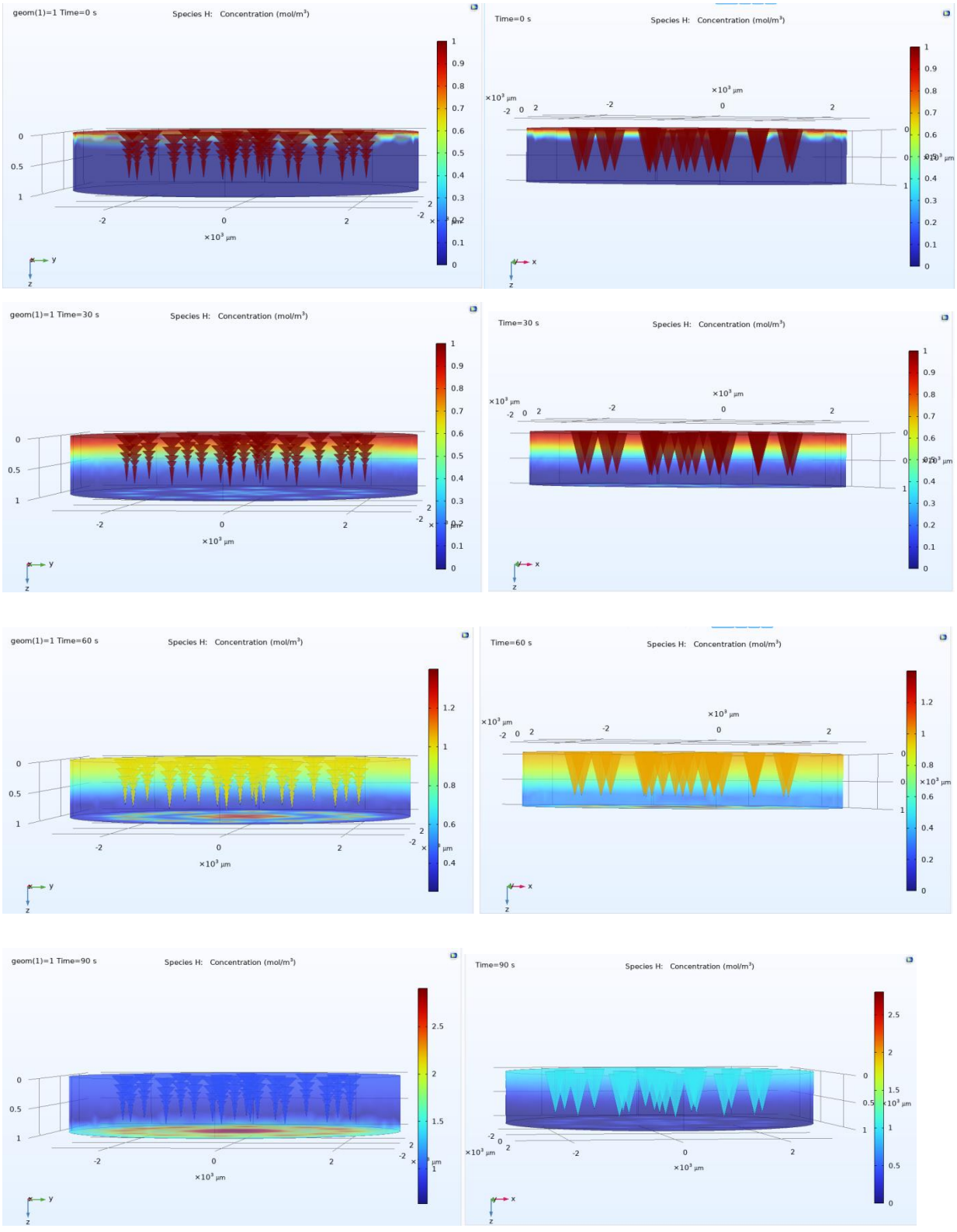
geom(1)=1 Time=0 s
Species H: Concentration (mol/m³)
Time=0 s
Species H: Concentration (mol/m³)
geom(1)=1 Time=30 s
Species H: Concentration (mol/m³)
Time=30 s
Species H: Concentration (mol/m³)
geom(1)=1 Time=60 s
Species H: Concentration (mol/m³)
Time=60 s
Species H: Concentration (mol/m³)
geom(1)=1 Time=90 s
Species H: Concentration (mol/m³)
Time=90 s
Species H: Concentration (mol/m³)

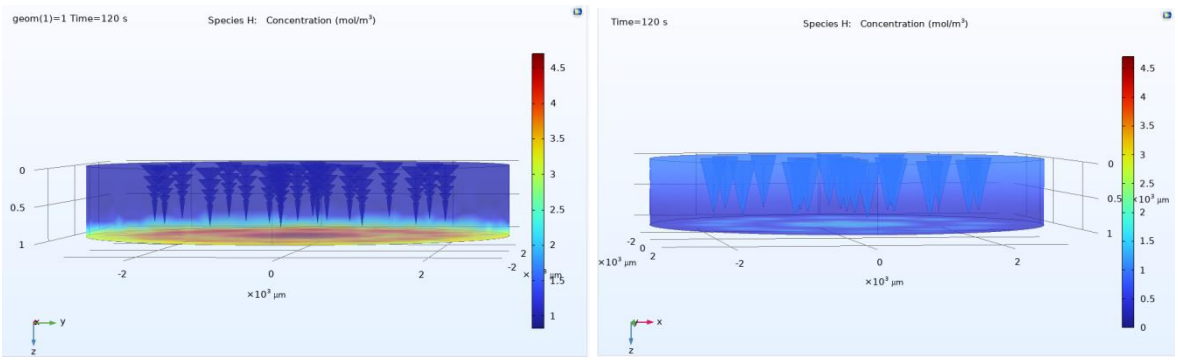


Figure 14: Comparison of charged species concentration simulated over varied time frames (0 s, 30 s, 60 s, 90 s, 120 s) between (a) bio-inspired and (b) cone MNs

Table 2: Parameters after creating channels with MNs (cone and bio-inspired MNs with 5 edges)

| | Cone MNs | Bio-inspired MNs with 5 edges | Description |
|---|---|---|---|
| Current | 3 mA | 3 mA | Current across 1 mm-thick skin |
| Max electric field | 50 V/m | 900 V/m | At the edges of bio-inspired MNs versus the surface of cone MNs |
| Max electrophoretic flux magnitude | $15\times10^{-6}$ mol/($m^2\times s$) | $35\times10^{-6}$ mol/($m^2\times s$) | After 120 s on opposite side of skin |
| Max concentration of charged species | 1.5 mol/$m^3$ | 4.5 mol/$m^3$ | After 120 s on opposite side of skin |
| Microchannel length | 1600 µm | 2400 µm | Length of created channels by MNs |

## 2-2. Validation and Modification of MN Geometry with ITP

Given the intricate design parameters and the multifaceted variables involved, we purposefully chose to authenticate our findings by replicating the experimental and numerical conditions as outlined in the previously cited study [96]. Our intent was to ensure the credibility of our results by closely emulating the simulation methodologies detailed in the referenced article

[96]. This validation process not only boosted our confidence in the accuracy of our simulated outcomes but also enabled us to investigate how alterations to MN geometry can impact our findings. This comprehensive approach forms the foundation of our exploration into the potential of bio-inspired MNs and ITP to revolutionize TDD. We've used insulin as a model drug to gauge the effectiveness of our microchannels in facilitating model drug transport. This configuration is displayed in Figure 15. The design comprises a solid MN array, medical tape, an anti-seepage gasket, and a medical sponge. The solid MN array is used to puncture the skin, creating microchannels in the SC layer and skin. This paves the way for passive diffusion of liquid drug formulation into the bloodstream. This process essentially involves three steps: 'coating, puncturing, and diffusion.'

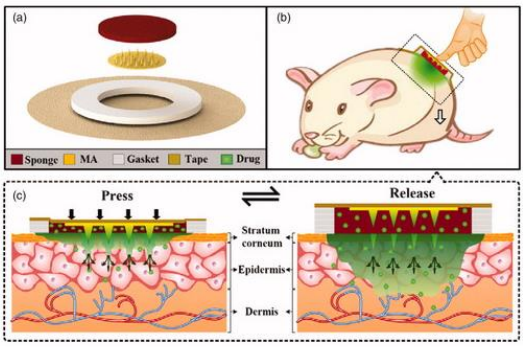


Figure 15: (a) Detailed visualization of transdermal MN array patch (TMAP) components. (b–c) Illustration depicting the drug administration approach of TMAP.[ 96]

We conducted a numerical simulation to model the diffusion of insulin using a TMAP via the COMSOL software with a specific focus on validating drug release mechanisms by evaluating drug concentration and release duration. For precise modeling, we referenced specific values from a related article [96].

The simulation model was established within the Electric Currents and Transport of Diluted Species physics modules. The simulation utilized Fick's first law of diffusion to calculate the steady-state flux (Jss) of a drug across the skin. The materials considered in the simulation included sponge, skin, MNs, air, and the SC. Assumptions were made, including an initial skin concentration of 0 mol/m$^3$, a drug diffusion coefficient through the skin of $1.2 \times 10^{-10}$ $\frac{m^2}{s}$, and a

diffusion coefficient of the SC as 0 $\frac{m^2}{s}$. Additionally, it was assumed that 100% of the MN surface area was in contact with the skin upon insertion. The drug delivery methodology applied in this study features a solid MN array adhering to the 'poke with patch' principle.

In this particular setup, we consider using solid MNs to gently penetrate the skin, allowing the drug from the sponge to be applied onto the skin's surface. Our simulation is divided into four domains: the outermost layer (stratum corneum), the epidermis, the sponge, and the microchannels. We've used specific parameters for this simulation, as outlined in Table 3.

Table 3: The specific parameters for numerical simulations [96]

| Parameters | Expression |
|---|---|
| Height_MN | 600 µm |
| Sponge_thickness | 1100 µm |
| Sponge_radius | 1500 µm |
| Skin_thickness | 2500 µm |
| Skin_radius | 2000 µm |
| SC_thickness | 15 µm |
| Base radius_MN | 90 µm |
| MNs number | 42 |
| Insulin concentration | 0.234 (5IU) $\frac{\text{mol}}{\text{m}^3}$ |
| Diffusion coefficient | $1.2\times10^{-10}$ $\frac{m^2}{s}$ |
| Duration | $4.32\times10^4$ s |

Our setup involves an array of 42 MNs organized together. The MN array used for this simulation is visually depicted in Figure 16(a). The MN array boasts a 12 mm substrate diameter, with needles uniformly spaced across it.

The boundary conditions are thoughtfully assigned to their corresponding borders, as illustrated in Figure 16(b):

**Boundary 1:** This delineates the MN/patch boundary, which governs insulin diffusion into the skin. Initially, this boundary holds a concentration of 0.234 (5IU) $\frac{\text{mol}}{\text{m}^3}$, which depletes over time as insulin migrates into the skin. Consequently, the flux condition here factors in drug diffusivity

through the patch and its remaining drug content. Cpatch0 aligns with insulin injection concentrations. The concentration entering the skin decreases over time.

**Boundary 2:** This boundary exclusively models insulin diffusion into the skin and capillaries, barring any outward drug migration along the x-axis. Hence, there's no drug flux in the x-direction, a condition we enforced.

**Boundary 3:** Here, voltage is applied to ensure constant current flow.

**Boundary 4:** Attached to the ground terminal, this boundary completes the design's electrical circuit.

Meshing of the skin, drug reservoir, and microchannels domain is shown in Figure 16(d). We employed a converged mesh consisting of free tetrahedral elements. The SC layer and microchannels are extremely fine meshed, yielding a very fine structure (indicated by black solid appearance). This fine mesh enhances precision in calculating drug concentration exiting the microchannels.

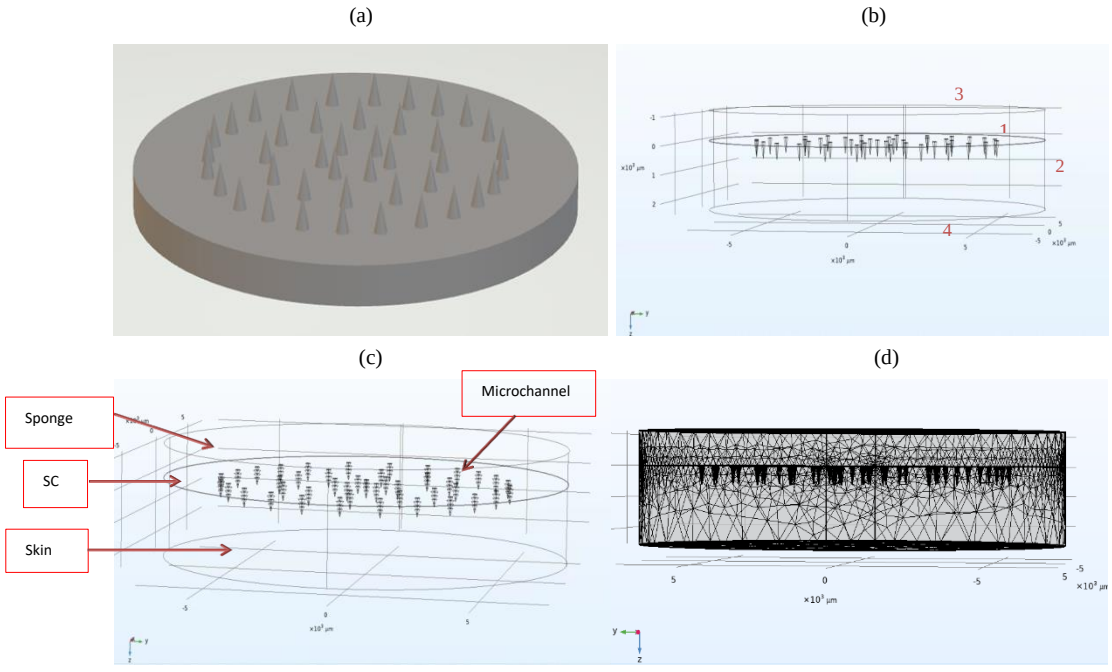


Figure 16: (a) MN array, (b) simulation model of touch-actuated cone MN array, (c) simulation model of touch-actuated MN array, and (d) the mesh model of touch-actuated MN array.

We embarked on an assessment of insulin concentration within the skin over a span of 43100 seconds concerning cone MNs, aiming to mirror the outcomes. Figure 17 provides insight with six surface plots detailing insulin concentration at selected intervals: 0, 900, 4300, 9000, 22000, and 43100 seconds. They were strategically chosen to illustrate the progression of insulin diffusion across the SC and epidermis throughout this period. Notably, the SC exhibits minimal diffusivity, causing insulin to diffuse more gradually through this upper layer compared to the underlying epidermis. Over time, the concentration at the microchannels gradually diminishes as insulin depletion from the patch influences this. The major portion of the drug enters the epidermis via the punctures. Remarkably, almost the entirety of the reservoir's drug reaches the skin by 22000 seconds, corroborating the congruity of our results with the referenced article. Figure 17 notably exhibits an immediate surge in drug concentration upon patch application, succeeded by a steadier ascent post-22000 seconds. The referenced article adopts solid cone MNs in their TMAP method, a 30-minute session attributed to microchannel shrinkage. Moreover, our simulations align closely with the article, registering a drug quantity of $3.3 \times 10^{-8}$ mol within the same timeframe, while the article reports around $3.4 \times 10^{-8}$ mol. This alignment bolsters the authenticity of our simulation outcomes, as shown in Figure 18.

| Time (s) | Reference [96] | Our results |
|---|---|---|
| 1 | 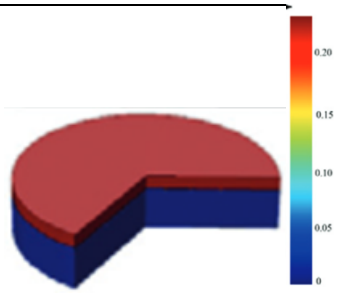 | 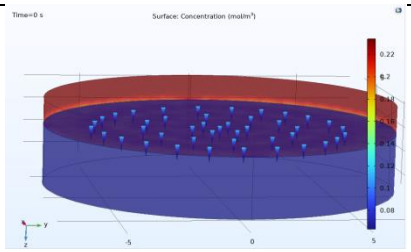 |
| 900 | 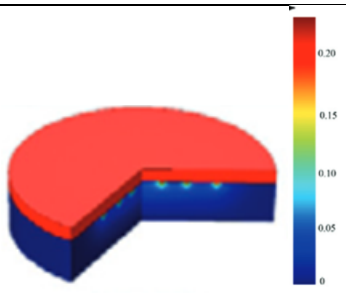 | 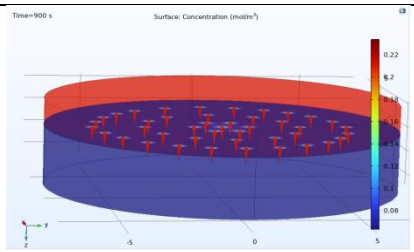 |

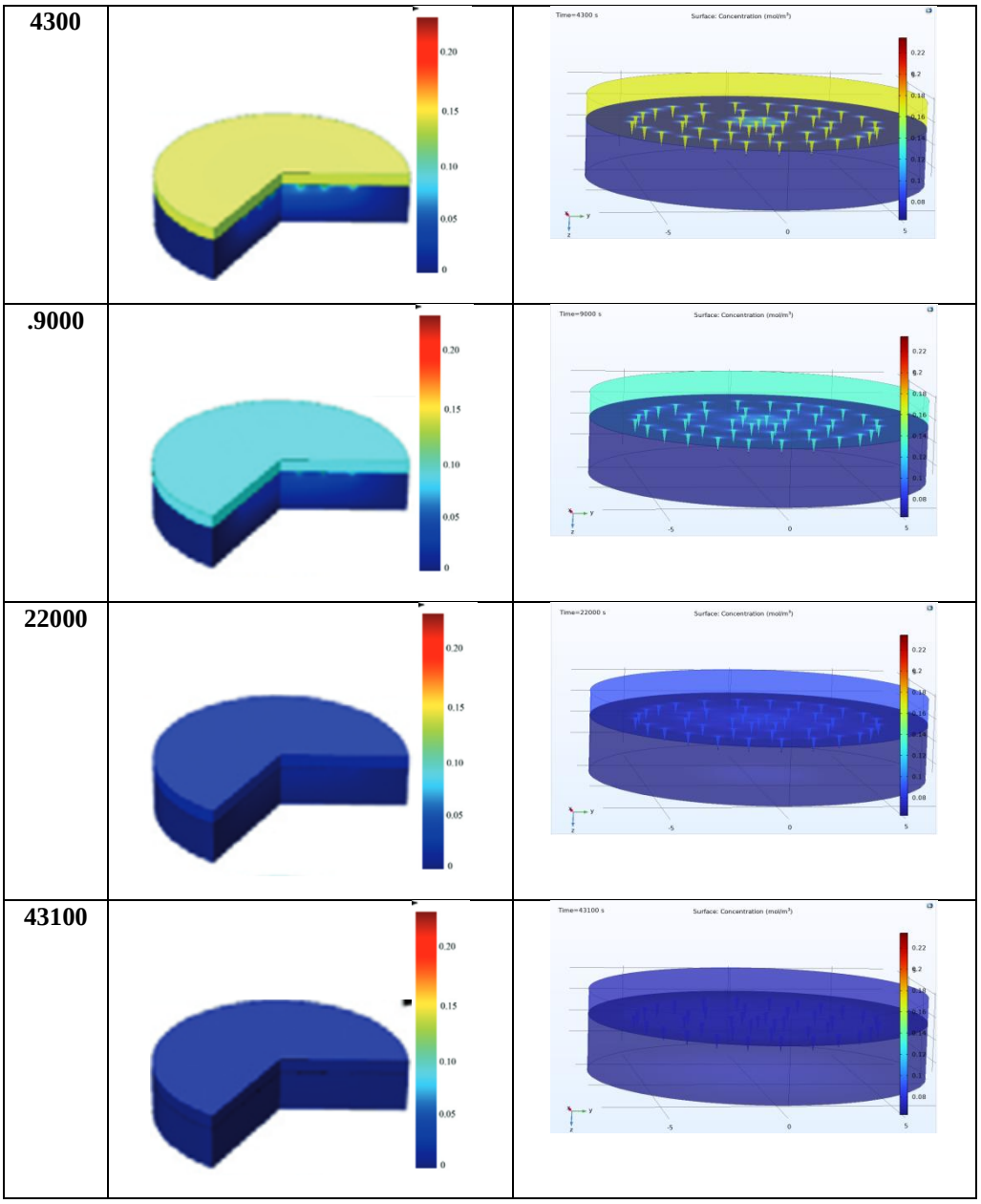


Figure 17: Comparative Analysis of COMSOL simulated results and the reference [96]: Skin concentration distribution during transdermal insulin delivery

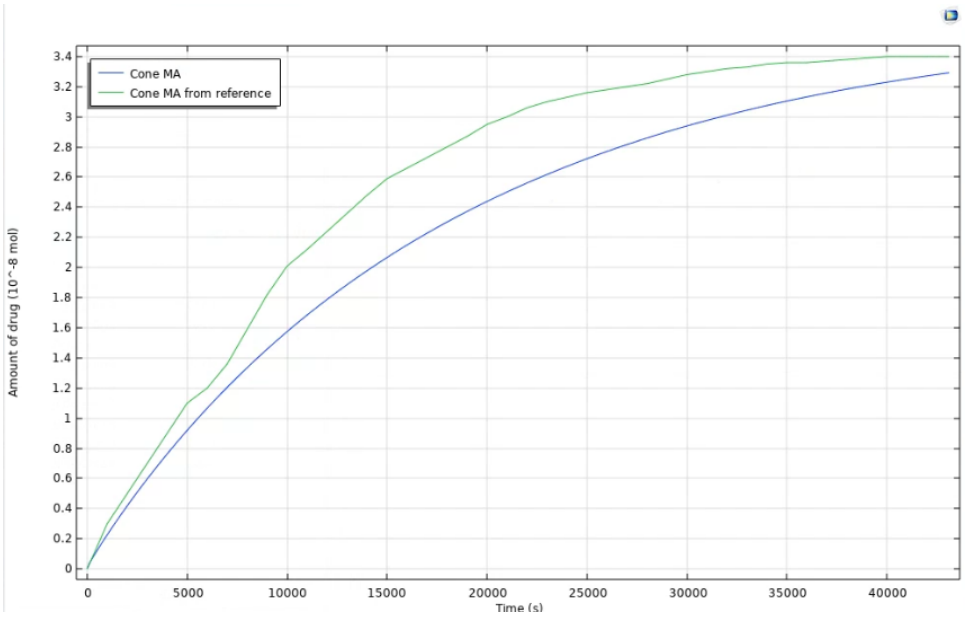


Figure 18: Comparative analysis of COMSOL simulated results and reference [96]: Total insulin diffusion amount.

Maintaining these parameters, we modified the microchannel geometry to observe its effects. Both MNs shared a base diameter of approximately 200 µm and stood at a height of approximately 600 µm. Notably, the bio-inspired MNs, as portrayed in Figure 19, uniformly exhibited barbs measuring 120 µm in height. Distinctive to the bio-inspired MNs, each one featured a configuration of five rows of fins extending longitudinally along its structure. The purpose behind these barbs was to augment the surface area coverage provided by the MNs. Initially, we aimed to incorporate a higher number of barbs to potentially enhance their efficacy. However, our endeavors to fabricate MNs with more than five barbs proved unsuccessful, resulting in the formation of unsatisfactory edges during the manufacturing process. Consequently, we determined that limiting the barbs to five emerged as the optimal configuration for our MN array measuring 600 µm in height. Furthermore, the MNs exhibiting five uniformly sized barbs showcased more well-defined edges, a characteristic particularly pronounced in the bio-inspired variants.

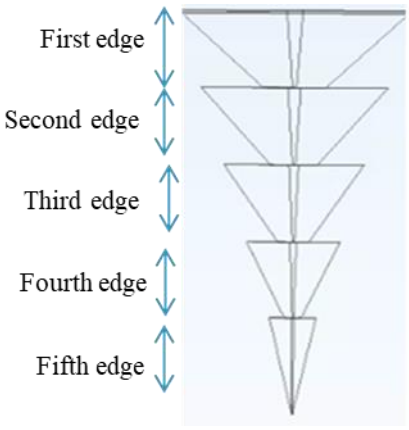


Figure 19: The definition of edges on bio-inspired MN

Table 4: Geometry parameters of bio-inspired MN with five edges

| **Name** | **Expression (μm)** | **Description** |
|---|---|---|
| BR-5 | 90 | Bottom radius of first edge on a bio-inspired MN |
| TR-5 | 100 | Top radius of first edge on a bio-inspired MN |
| BR1-5 | 135 | Bottom radius of second edge on a bio-inspired MN |
| TR1-5 | 85 | Top radius of second edge on a bio-inspired MN |
| BR2-5 | 120 | Bottom radius of third edge on a bio-inspired MN |
| TR2-5 | 65 | Top radius of third edge on a bio-inspired MN |
| BR3-5 | 95 | Bottom radius of fourth edge on a bio-inspired MN |
| TR3-5 | 30 | Top radius of fourth edge on a bio-inspired MN |
| BR4-5 | 50 | Bottom radius of fifth edge on a bio-inspired MN |
| TR4-5 | 0 | Top radius of fifth edge on a bio-inspired MN |
| Edge_height | 120 | The height of each of the five edges on a bio-inspired MN |
| Total_height | 600 | Total height |
| Base_radius | 90 | Base radius |

Furthermore, the interplay of current was investigated. We explore drug delivery under two conditions: with and without the application of an electric current. The modification of this MN array's geometry aims to enhance drug delivery via ITP. To observe changes in the results, a consistent electric current is applied between the drug reservoir and the skin. In our modeling of insulin MNs using COMSOL, we establish a series of assumptions to streamline computation and simulate an idealized scenario:

1. Convection is neglected, with diffusion and electrophoretic flux constituting the primary mass transport mechanisms.
2. Migration within an electric field and mass transfer in porous media are deemed the prevailing transport mechanisms.
3. The exerted pressure from MN application will not influence drug delivery within the skin.
4. A constant current is maintained between the sponge and skin.
5. Insulin diffusion into the skin occurs via the MN-created pores, originating from the sponge.
6. The presence of skin hair is disregarded.
7. Electric field interactions impact space charge density, and vice versa.
8. Drug delivery employs the "poke and patch" methodology.

Figure 20 reveals a remarkable finding: 1) The concentration analysis demonstrates that bio-inspired MNs, particularly those with 5 edges, result in higher insulin concentrations within the skin compared to their cone-shaped counterparts. 2) The concentration of insulin reaches its zenith when bio-inspired MNs with 5 edges are coupled with current between the reservoir and the skin. This phenomenon can be attributed to the augmented surface area of the microchannels and the intensified electric field engendered by the edges of the bio-inspired MNs. Conversely, the cone MNs without current exhibit the lowest concentration levels.

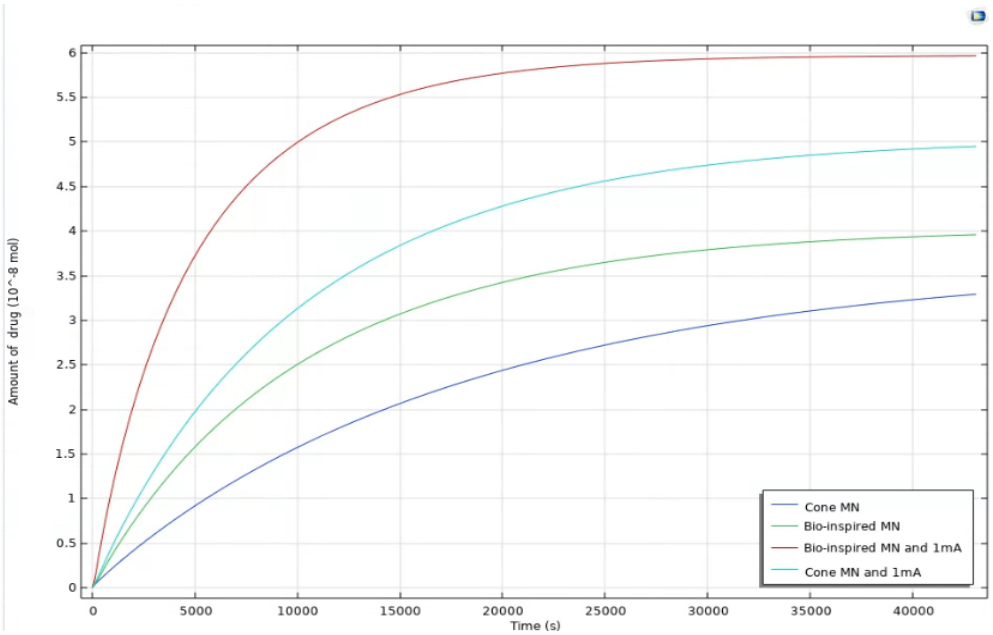


Figure 20: COMSOL-simulated transdermal insulin delivery results. Total drug amount delivered using different MNs (cone and bio-inspired with 5 edges), with/without 1mA current.

Based on the outcomes obtained, it can be deduced that our hypothesis regarding the efficacy of employing bio-inspired MNs in combination with ITP for enhanced drug delivery is validated.

# Chapter 3: Materials and Methods

The primary objective of this experimental study is to elucidate and evaluate the efficacy of combining MN technology with ITP for enhanced delivery using dye as a proof of concept. Central to this investigation is the alteration of MN geometry, transitioning from the conventional cone MN design to the bio-inspired MN. This modification holds the potential to augment the electric field due to the presence of barbs on the bio-inspired MN structure. Moreover, the increased surface area of the bio-inspired MN is expected to induce observable changes in the microholes generated by these MNs within the delivery matrix.

The anticipated outcomes involve a discernible increase in the penetration depth of the model drug when employing the combination of bio-inspired MNs and ITP over time. This assessment will be indicative of the superior performance achieved through this amalgamation, potentially leading to enhanced drug delivery across skin barriers.

Conversely, when reverting to the use of cone MN arrays, it is anticipated that a reduced penetration depth will be observed. Detailed findings and comparative analyses delineating the varying degrees of penetration depths between bio-inspired and cone MN configurations will be presented comprehensively in the subsequent sections. A detailed breakdown of the experimental outcomes and comparative analyses is provided in the accompanying table, offering a comprehensive insight into the observed variations in penetration dynamics between different MN geometries and ITP.

In the upcoming section, a detailed exploration of various critical components will be undertaken. The segment will commence by intricately examining the design and fabrication aspects of MNs. This will encompass the inventive design concepts behind two distinct MN types: cone-shaped and bio-inspired MNs, emphasizing their geometric specifications, array arrangements, and the manufacturing intricacies involved in their fabrication. Following this, the exploration will extend to the experimental investigations involving bio-inspired and cone MN tests. These tests will encompass an in-depth elucidation of skin anatomy, the creation of an agarose gel and parafilm-based skin model, and an exploration into the movement of charged particles within a gel matrix under the influence of an electric field. Subsequently, the focus will shift towards the results and discussions derived from the aforementioned experimental endeavors.

This will include an analysis of the dye delivery mechanism elucidating the synergy between MNs and ITP, and a comprehensive discussion of the outcomes from dye delivery experiments exploring the influence of different MN configurations on model drug permeation rates and the intricate mechanisms driving dye delivery.

## 3-1. Design and Fabrication

### 3-1-1. MN Design

In the previous chapters, we introduced the foundational principles guiding this research project. Our primary objective is the development of a novel class of MNs through a bio-inspired methodology aimed at medical applications. This initiative is inspired by earlier discussions on parasites, with a particular focus on emulating their hook or fin-like structures. This section comprehensively delves into our inventive design concepts and their realization.

Our development process yielded two distinct types of MNs: cone-shaped and bio-inspired variants. The bio-inspired MNs feature minuscule barbs projecting horizontally from their surfaces. These MNs were meticulously organized in an array consisting of 42 individual units, as visually represented in Figure 21. The arrangement was executed atop a circular base or substrate, possessing a thickness measuring 1000 micrometers.

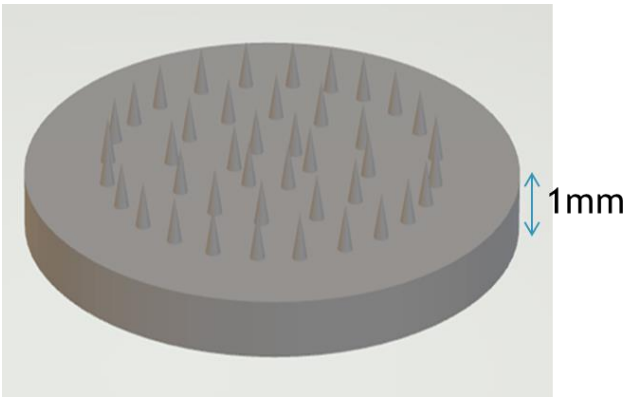


Figure 21: An array of precisely arranged solid MNs, consisting 42 MNs.

Both MNs shared a base diameter of approximately 200 micrometers and stood at a height of approximately 600 micrometers. Notably, the bio-inspired MNs, as portrayed in Figure 22, uniformly exhibited barbs measuring 120 micrometers in height.

Distinctive to the bio-inspired MNs, each one featured a configuration of five rows of fins extending longitudinally along its structure. The purpose behind these barbs was to augment the surface area coverage provided by the MNs. Initially, our experimentation aimed to incorporate a higher number of barbs to potentially enhance their efficacy. However, our endeavors to fabricate MNs with more than five barbs proved unsuccessful, resulting in the formation of unsatisfactory edges during the manufacturing process. Consequently, we determined that limiting the barbs to five emerged as the optimal configuration for our MN array measuring 600 micrometers in height. Furthermore, the MNs exhibiting five uniformly sized barbs showcased more well-defined edges, a characteristic particularly pronounced in the bio-inspired variants.

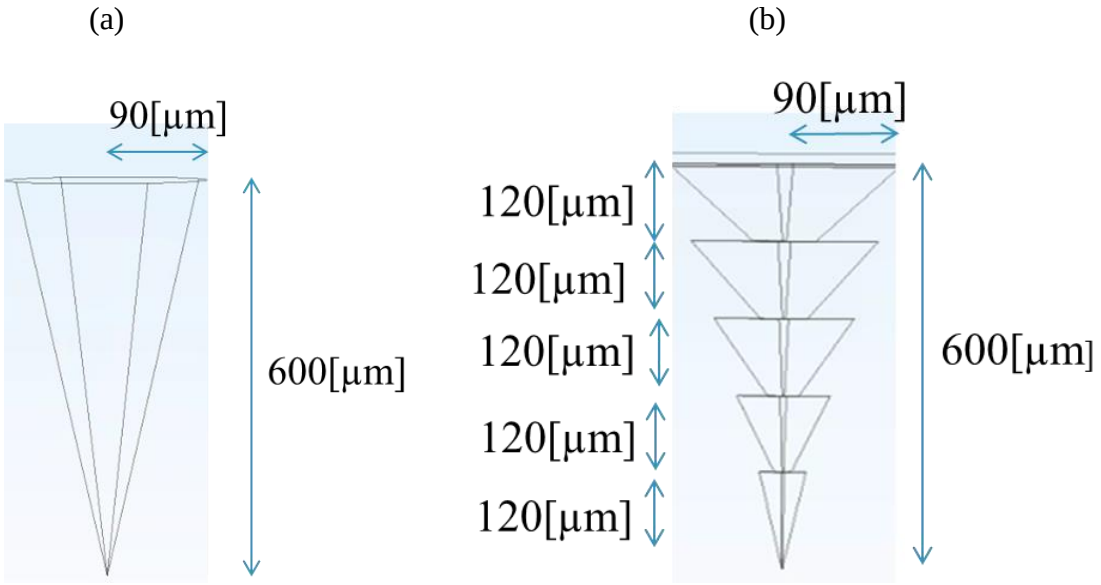


Figure 22: Comparison of the design and measurements of a) Cone MN and b) Bio-inspired MN models.

## 3-1-2. MN Fabrication

The initial step in the fabrication process involves the conversion of the MN model into a stereolithography (STL) format. This STL file is subjected to slicing procedures, employing a specified layer thickness to generate 2D cross-sectional images. These images are compressed into

a file that can be read by a 3D printer. At the printer, each of these images is meticulously transmitted to an LED panel one after the other, enabling the generation of a light pattern. This pattern is then projected onto a surface that's been coated with liquid resin, initiating a specific curing period aimed at inducing crosslinking.

Once a layer solidifies, the stage descends, and fresh material is replenished on the surface. Subsequently, for the next layer, the stage ascends, moving precisely by a distance equivalent to the layer's thickness from its original position. This repetitive process persists until a complete 3D structure emerges (as seen in Figure 23) [97].

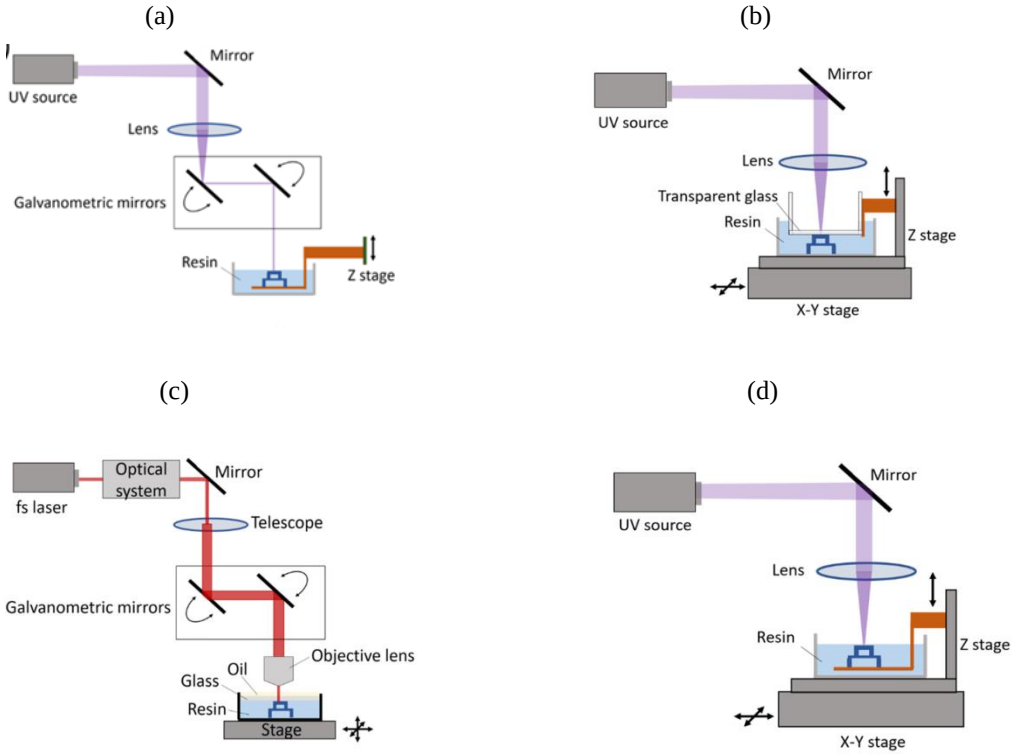


Figure 23: Scanning stereolithography processes. (a) Scanning stereolithography employing a dynamic light beam. (b) The constrained surface methodology. (c) The freeform surface approach. (d) A typical setup for two-photon polymerization (2PP) [97].

The specifications of the 3D printer highlight its exceptional resolution capability, boasting a detailed precision of 22 micrometers in the X and Y axes and 10 micrometers in the Z axis. This

signifies the printer's capacity to intricately reproduce fine details and intricate designs with a high level of accuracy in the horizontal plane (X and Y) and a remarkable level of layer thickness control in the vertical plane (Z). The 22-micrometer resolution in the X and Y axes denotes the printer's ability to reproduce fine details and intricate features with precision, contributing to the fidelity and accuracy of the printed objects' surface details. Meanwhile, the 10-micrometer resolution in the Z axis indicates the printer's capability to generate very thin layers, facilitating smoother and more detailed vertical surfaces in the printed objects. This level of precision and layer thickness control is beneficial for creating highly detailed and complex models or prototypes, catering to applications that demand exceptional intricacy and precision in three-dimensional printing.

A separate 3D model, featuring a MN array characterized by triangular-shaped fins, was meticulously designed and subsequently transformed into the STL format (as seen in Figure 24). Following this, the STL file was subjected to the slicing process to generate 2D cross-sectional images. Moreover, a detailed text file was generated, stipulating the curing duration and layer thickness pertaining to each image.

The printing sequence for the MN arrays involves the initial fabrication of the rectangular base or substrate, followed by the construction of the MNs themselves. Upon the completion of the entire MN structure, the support framework is removed.

Figure 25 presents microscopic images illustrating the MN structure, specifically showcasing the fabricated MN sample.

The conjecture underpinning our fabrication approach is centered on enhancing the adhesive performance of the MNs. We hypothesized that MNs featuring fins would demonstrate superior interlocking capabilities with biological tissues, consequently exerting higher adhesion forces during the extraction process. To validate this hypothesis, the actual dimensions of all fabricated features are meticulously compared against the initially designed specifications. This meticulous comparison serves to elucidate any disparities between the fabricated and intended dimensions, providing crucial insights into the fabrication process's precision and performance. The collective focus on design and fabrication was directed towards crafting MNs inspired by nature's efficiency

and robustness. This endeavor holds promise for enhancing their potential applications in various biomedical fields.

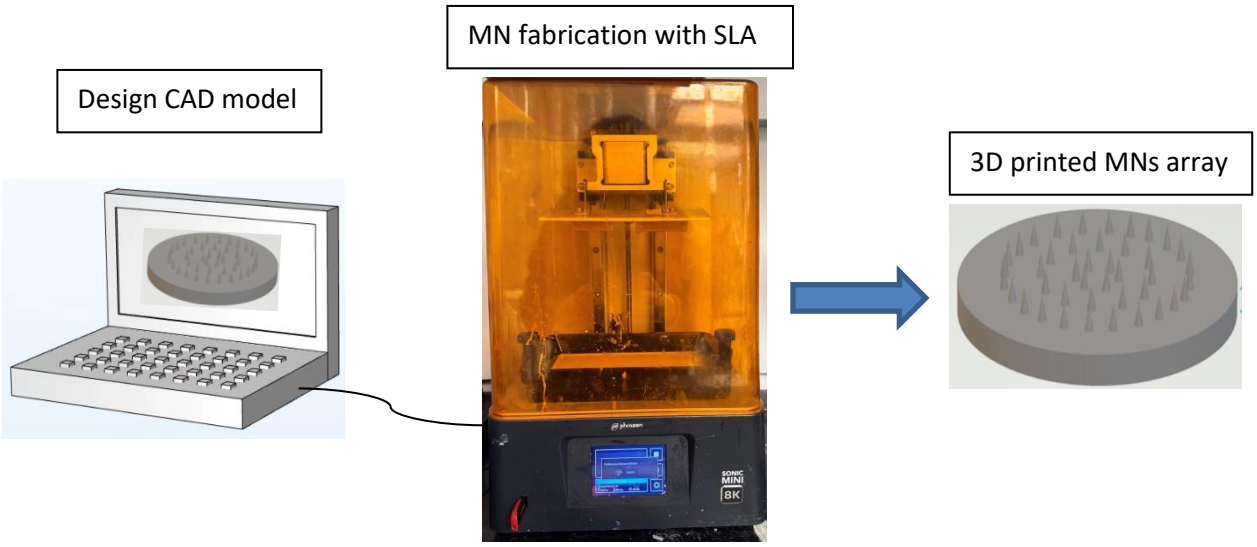


Figure 24: a MN array design followed by 3D printing of the design.

(a) (b)

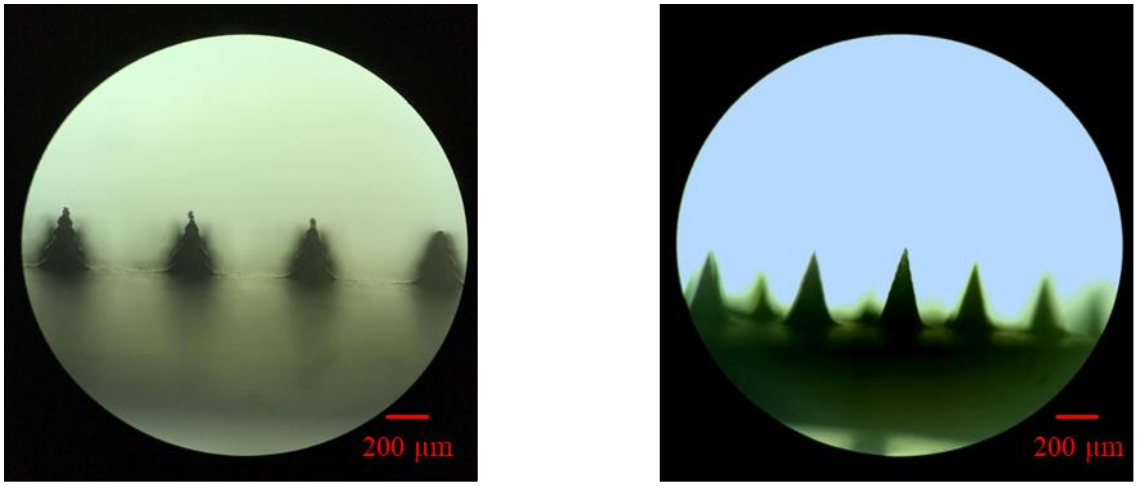

(c) (d)

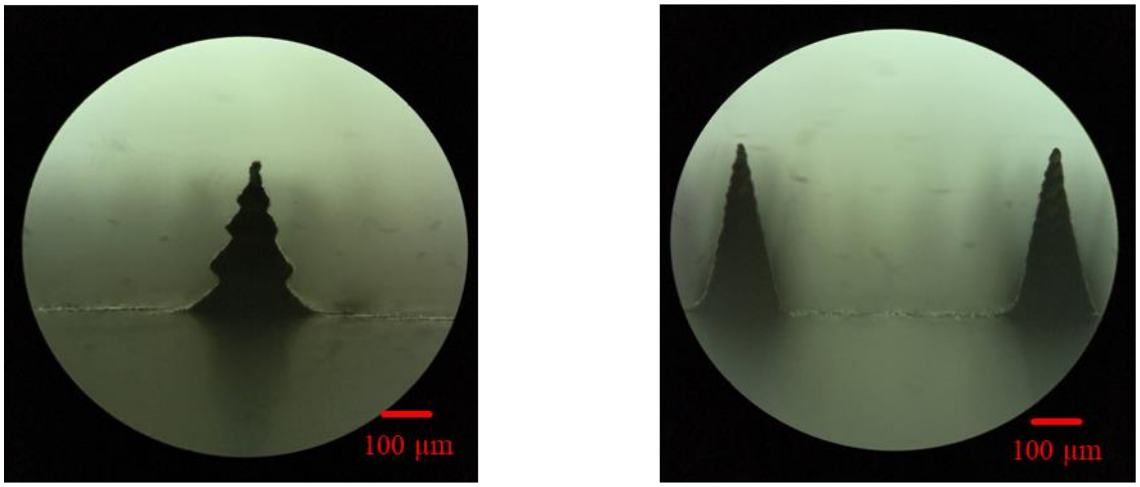


Figure 25: Optical images of fabricated (a) bio-inspired MN array, (b) cone MN array, (c) one bio-inspired MN, and (d) two close cone MNs.

## 3-2. Bio-inspired and Cone MN Tests

### 3-2-1. Skin Anatomy

Understanding the composition of the skin is vital before delving into MN penetration testing. An illustration, depicted in Figure 26, elucidates the microanatomy of the skin, highlighting its three primary layers: the epidermis, dermis, and hypodermis, each playing a unique role in the skin's structure and function.

The epidermis, the outermost layer, encompasses the SC, responsible for shielding the skin. This particular region exhibits considerable stiffness, typically ranging from 50 µm to 150 µm in thickness. Beneath the epidermis lies the dermis, significantly thicker than the epidermis with a typical thickness ranging from 500 µm to 2000 µm. The dermis houses a vast network of capillary tubes and nerve endings, making it a vital area for transdermal applications, especially for blood sample extraction. Finally, the hypodermis, the deepest layer, boasts a thickness higher than the

other two layers (approximately 30000 μm) but exhibits lower stiffness compared to the upper layers.

This distinction in layers, characterized by varying thicknesses and stiffness, contributes to the skin's overall function and responsiveness. Understanding these layers is crucial in developing skin models for penetration testing, allowing for the accurate replication of skin properties for experimental analysis and evaluation.

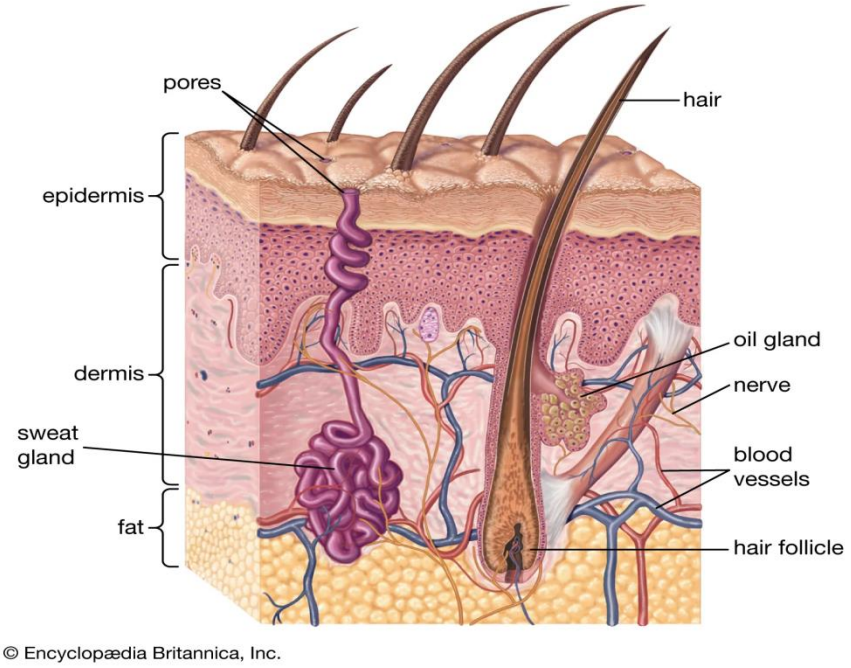


Figure 26: The microanatomy of the skin with several layers: epidermis, dermis, and hypodermis [98].

### 3-2-2. Skin Model: Agarose Gel and Parafilm

To replicate the protective characteristics of the skin's SC, given that actual skin is not used in our experiments, we employ a methodology using parafilm layered on top of agarose gel. This arrangement serves as a skin model for our penetration testing, aiming to mimic the barrier properties of the SC. To stretch the parafilm, we utilize adhesive foam as a substrate, effectively fixing and elongating the parafilm, as visually demonstrated in the accompanying Figure 27.

Figure 27: Parafilm (transparent) attached to the adhesive foam (black) as model for SC .

Once the parafilm is stretched and adhered onto the adhesive foam, we carefully position this composite layer onto the agarose gel reservoir, which previously received a solution of dissolved agarose. Agarose gel, recognized as an in vitro model simulating skin, is derived from a white powder that dissolves in near-boiling water (melting temperature: 85-90 °C) and solidifies into a gel when cooled (gelling temperature: 34-38 °C).

The preparation of the agarose gel involves meticulous steps. For instance, for a 1% agarose gel concentration, we mix 7.5 mL of 1X Tris/Borate/EDTA (TBE) Buffer with 75 mg of agarose powder. This formulation achieves the desired 1% weight percentage of agarose. The dissolution process begins by placing the agarose powder and TBE buffer inside a water beaker mounted on a hot plate with a magnetic stirrer. By setting the temperature to 200 °C and activating the stirrer, a water bath is created, facilitating the dissolution of the powder into the TBE Buffer. This process typically takes 15-20 minutes, ensuring the complete dissolution of the agarose powder, resulting in a clear solution. The detailed depiction of this dissolution process within a water bath is provided in the corresponding Figure 28.


Figure 28: Dissolution process of agarose powder in TBE buffer illustrated within a water bath setup.

Subsequently, this dissolved agarose solution is meticulously poured into a mold specially designed using 3D printing technology to accommodate and retain the gel. The poured solution is then left undisturbed in the mold, allowing it to undergo the transition from a liquid state to a gel. This crucial phase ensures the formation of a solidified gel structure replicating the properties of the skin model we aim to simulate for our experiments.

## 3-2-3. Electric Field-Driven Movement of Charged Particles in Gel

In this study, we conducted an investigation into the movement of charged particles within a gel under the influence of an electric field. To accomplish this, we employed the "poke and patch" method to facilitate the transfer of charged particles. Initially, pressure was applied to create MN-induced holes in an agarose gel. Subsequently, a 1 mA current was directed between positive and negative terminals to drive the transfer of charged particles through these MN-generated apertures. Conducting a comparative analysis of the agarose gels subsequent to the tests holds significant promise in elucidating the intricate influence of MN geometry specifically in the context of ITP-driven particle transfer mechanisms. Visual examination and comparison of agarose gel images

obtained via confocal laser microscopy after conducting these tests enable a deeper understanding of how charged particles navigate through the gel under different conditions.

The experiments were designed to study how the shape of MNs affects the way medicines are delivered using ITP. This investigation involved the use of two types of MNs. The strategy employed here combines the use of MNs with ITP for dye and acid delivery purposes. A constant current was applied between the MN and the negative terminal in this configuration. Figure 29 provides a visual representation of the negative terminal, positive terminal, MN array, sponge, agarose gel, parafilm, and agarose gel reservoir utilized in the experimental setup.

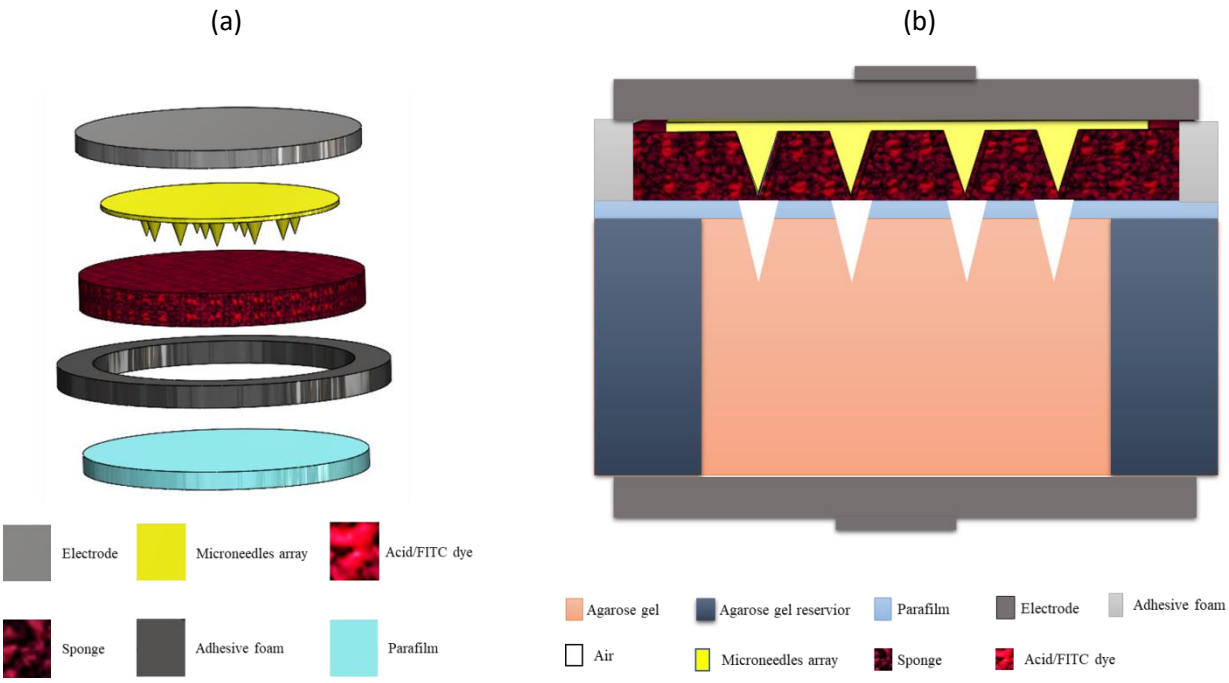


Figure 29: Schematic illustration of delivery system. (a) key components: electrodes, MNs array, Acid/FITC dye, sponge, adhesive foam, and parafilm, (b) experimental setup components: agarose gel, agarose gel reservoir, parafilm, electrode, adhesive foam, air, MNs array, sponge, acid/FITC dye. It operates via a voltage source providing constant current, maintaining stable current for ITP.

The performance of the bio-inspired MN array concerning model drug diffusion was thoroughly investigated, juxtaposed against the solid cone MN array. The experimental procedure involved several steps:

1. A model drug solution comprising 10 µL of FITC (Fluorescein Isothiocyanate) dye and acid was used, filling the pores of a sponge.

   The sponge, laden with FITC dye, was affixed onto the agarose gel surface, followed by a "press and release" action to initiate diffusion. The sponge is porous and contains numerous micropores, and it is employed as the reservoir of the IMAP, which can be filled with large doses of dye and acid formulations. The model drug diffusion process continued for a duration of 10 minutes while applying an electric current. For the solid MN array, the 'poke with patch' approach was implemented. The solid MN array was pressed into the gel under compression force, creating micropores. Subsequently, a dye-loaded patch was placed over the punctured gel for 10 minutes while a constant current flowed between the positive and negative terminals.

(a)

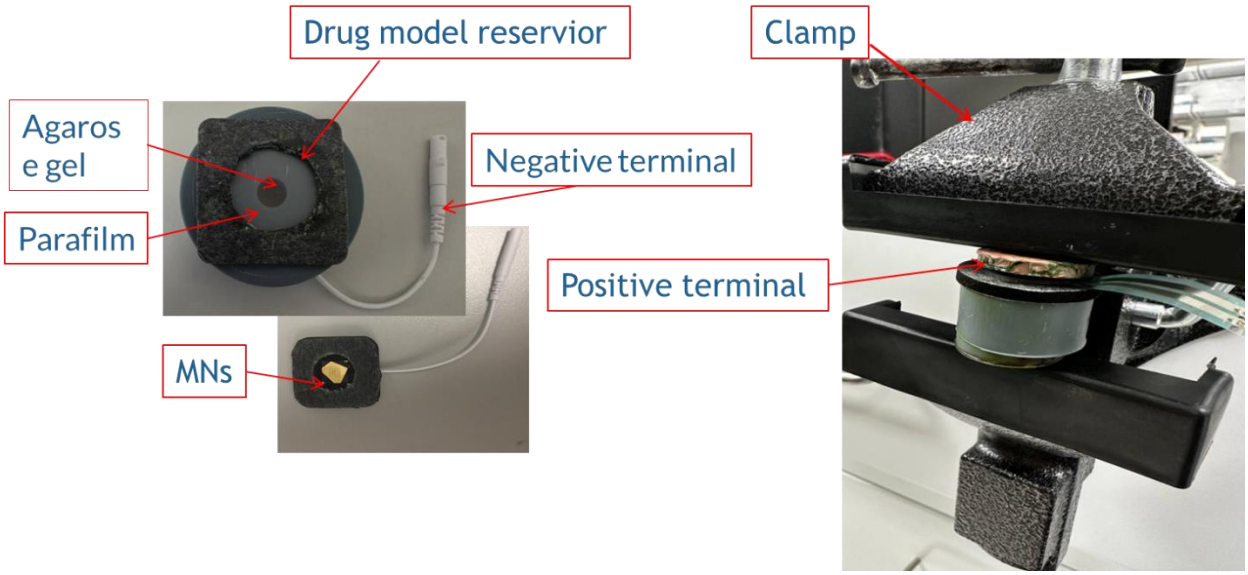

(b) (c)

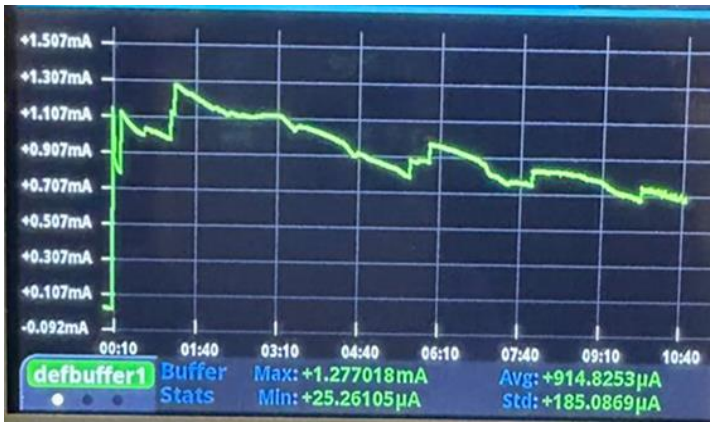


Figure 30: (a) Setup of the experimental arrangement illustrating in-vitro dye/ acid delivery utilizing a combined MN array and ITP. Components shown include: parafilm, agarose gel, agarose gel reservoir, negative terminal, positive terminal, MN array, drug model reservoir, and clamp. (b) Illustration of the constant current source. (c) Plot depicting the application of a constant current between positive and negative terminals over a duration of 10 minutes.

2. Confocal laser scanning microscopy was employed to examine these gel samples that had undergone diffusion with the dye for further detailed investigations.

A testing setup system was deployed to scrutinize the MN penetration process while simultaneously applying a 1 mA constant current over a duration of 10 minutes, as illustrated in Figure 30. This setup allowed for the meticulous observation and analysis of the model drug diffusion and movement of charged particles within the gel under varying conditions.

# Chapter 4: Results and Discussion

## 4-1. Dye/acid Delivery Mechanism

The intricate development of a sophisticated dye delivery system focused on facilitating both diffusion and ITP of a model drug solution. This system is an amalgamation of critical components: a constant current source, two electrodes, and an ITP-MN array patch (IMAP). One of the electrodes, in direct connection with the dye/acid solution, acts as an anode, specifically tailored for the ITP process. An anti-seepage foam has been adeptly integrated into the system to prevent any solution leakage from the sponge during gel penetration.

Central to this setup is the MA nestled within the medical sponge, playing a pivotal role in gel penetration. The MA creates micro-scale apertures, facilitating transdermal diffusion and ITP of the dye. Stability of voltage input and outputting a consistent current for effective ITP is ensured by the constant current source. The ITP-MN array comprises an electrode, parafilm, adhesive foam, a MN array (MA), and a sponge, meticulously arranged within concentric bonds. The porous nature of the medical sponge enables it to accommodate a substantial volume of solution. Additionally, the system's elasticity, owing to the properties of the sponge and foam, renders it compressible. The MA promote gel and parafilm penetration, subsequently detaching to facilitate seamless diffusion and ITP of the solution.

The systemic administration protocol of this system, termed "Penetration, Diffusion, and ITP," is multifaceted:

1. Gel penetration by the MA: Application of pressure to the IMAP initiates the penetration of the MA into the sponge reservoir, disrupting the parafilm and transiently creating aqueous microholes. Upon release of the IMAP compression, the inherent elastic rebound energy causes the MA to retract into the sponge.

2. Passive diffusion: Microholes generated by the MA are directly exposed to the drug model solution within the sponge. According to Fick’s law, the solution passively diffuses into the gel through these aqueous microholes. The rate of this diffusion is largely determined by microhole density and drug solution concentration, detailed in Figure 31.

3. Active ITP: A mild electric current is established between the electrodes, propelling charged therapeutic molecules through the microholes into systemic circulation via electromigration and electroosmosis. The quantity of transported therapeutic molecules is influenced by factors such as the molecules' charged potential, gel barrier modifications due to the MA, applied electric field intensity, and duration.

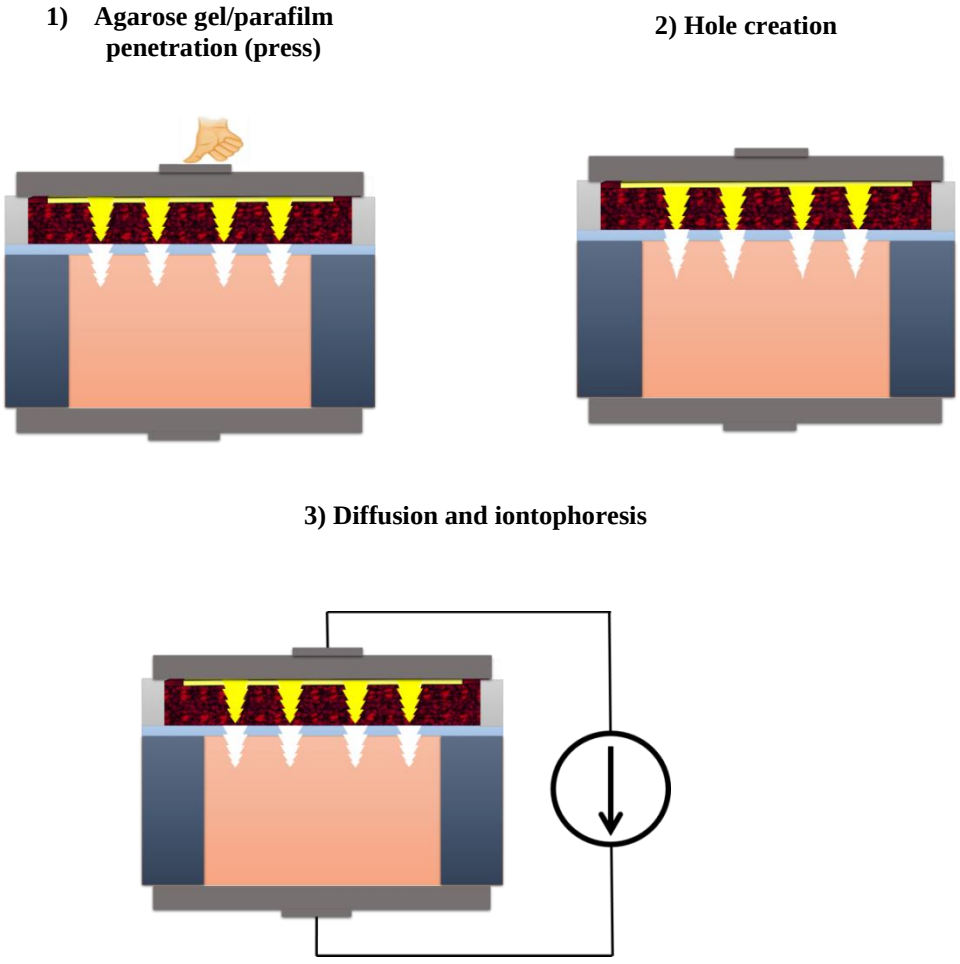


Figure 31: Illustration of the acid/dye delivery mechanism: 'Penetration, Diffusion, and ITP.' Pressure forms holes in the gel. Upon release, the MA retracts, allowing passive diffusion of the solution through micro-holes. Active ITP propels charged molecules into systemic circulation via electric current.

## 4-2. Dye/acid Delivery Results and Discussion

Notably, ITP is complemented by bio-inspired MNs rather than cone MNs to enhance model drug penetration, as elaborated in Figure 32. This system offers four distinctive model drug administration strategies, involving diverse combinations of model drug diffusion and ITP across the poked gel using cone MNs and bio-inspired MNs. The IMAPs under different usage conditions were divided into four groups (Cone MA, Cone MA/ 1 mA, Bio-inspired MA, Bio-inspired MA/ 1 mA). The effectiveness of this model drug delivery strategy, which combines positive diffusion and active ITP utilizing various MN types, will be comprehensively explored in subsequent sections.

A robust and efficient model drug delivery mechanism demands precise control over dye and acid diffusion. To comprehensively assess this, a series of in vitro permeation experiments were meticulously conducted using an agarose gel matrix. These experiments utilized various configurations of the IMAPs, stratified into four distinct groups: Cone MA group, Cone MA/1 mA group, Bio-inspired MA group, and Bio-inspired MA/1 mA group. A comprehensive breakdown of each group's specifications visual representations are elucidated in Figure 32.

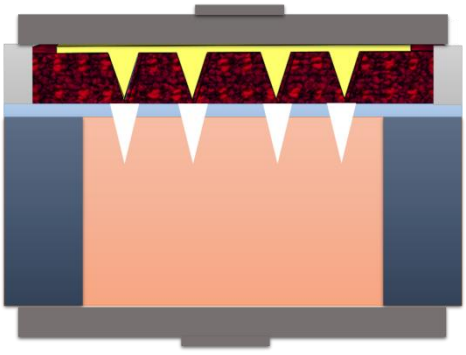

FITC Dye and acid/Cone MA

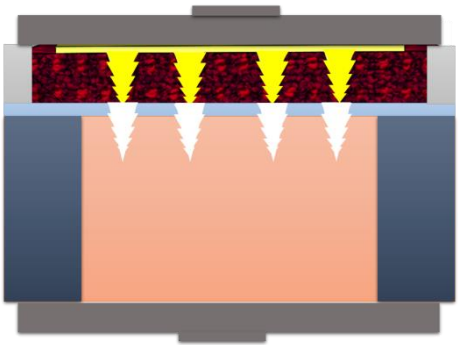

FITC Dye and acid/Bio-inspired MA

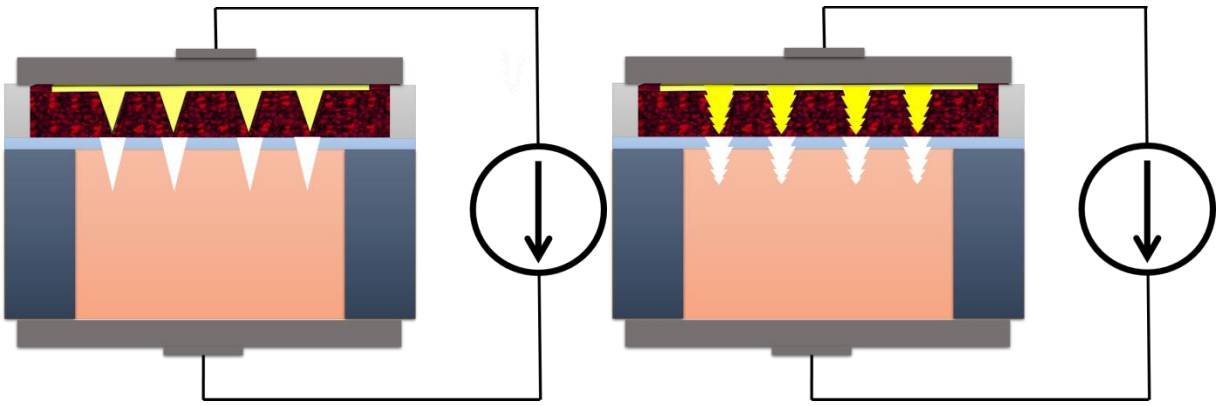

FITC Dye and acid/Cone MA/1mA

FITC Dye and acid/Bio-inspired MA/1mA

Figure 32: Schematic illustration of four groups operating under varied conditions

The strategic creation of microscale apertures by the MNs has proven to be a transformative measure in breaching the gel barrier, resulting in a substantial augmentation in the permeation rates. This notable enhancement can be attributed to the positive influence of electroosmosis and electrostatic interactions. Additionally, the cumulative permeation quantity exhibits an almost linear correlation with the intensity of the applied electric field. This remarkable relationship underscores the synergistic interplay between the MA and ITP, significantly aiding in the facilitation and regulation of model drug delivery dynamics.

The efficacy of ITP in transporting charged species and dyes across the skin's SC is pivotal. The electrophoretic force during ITP facilitates this process, while electrostatic attraction between the gel and charged species in the acid further augments the solution's permeability coefficient.

The cumulative effect of the MA and ITP manifests remarkably in expediting model drug delivery. This outcome reinforces the notion of enhancing model drug permeation rates through ITP, indicating the feasibility of a responsive and facile model drug administration process.

Confocal reconstruction images depicting different cross-sections of the agarose gel treated with various IMAP configurations (Cone MA group, Bio-inspired MA group, Cone MA/1 mA group, and Bio-inspired MA/1 mA group) for a 10-minute administration are delineated in Figures 33-36. Notably, the diffusion of the model drug through microholes created by the cone MA significantly enhances permeation, reaching a depth of approximately 1000 μm, even without the application of ITP, as evidenced in Figure 33. Similarly, the bio-inspired MA-created microholes

allow for model drug diffusion to deeper layers, enhancing permeation up to ~1400 µm without ITP, as illustrated in Figure 34. Higher fluorescence intensity, observed specifically in microholes created by the bio-inspired MA, signifies a more extensive diffusion of the model drug solution into deeper gel layers facilitated by these microholes.

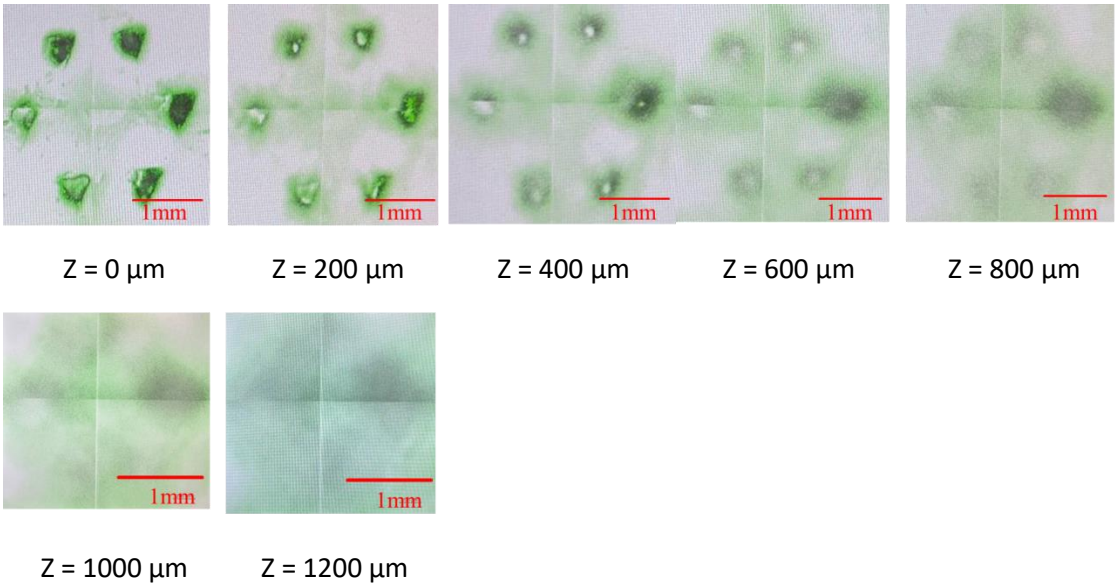


Figure 33: In vitro acid/dye delivery employing IMAP with cone MN array and without current application

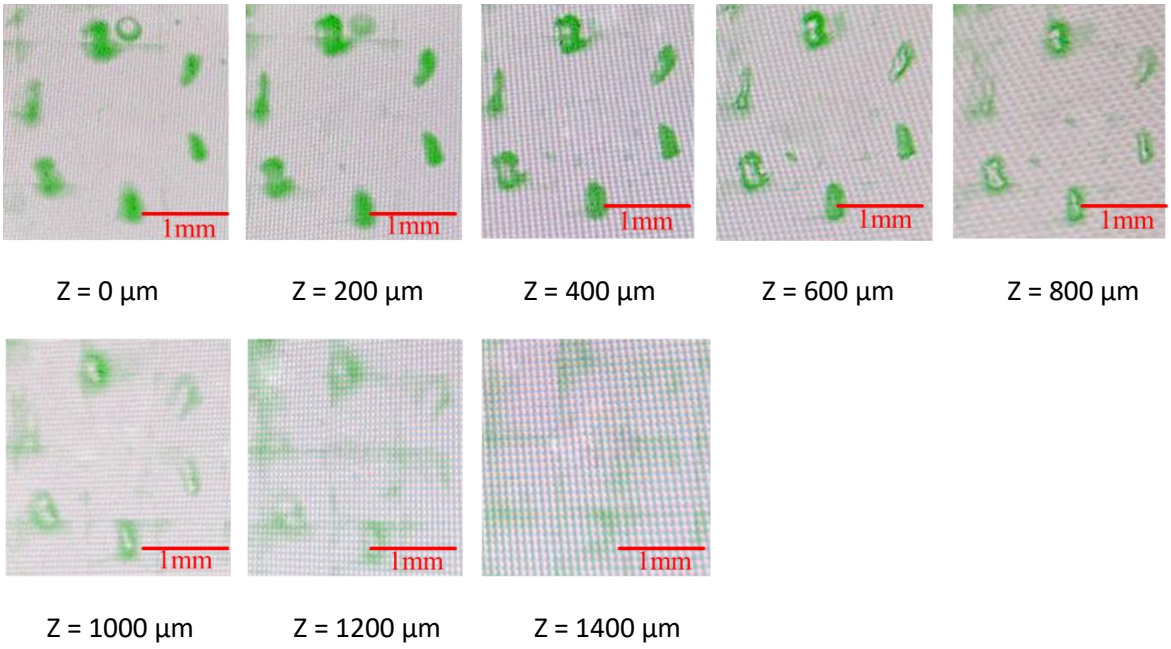


Figure 34: In vitro acid/dye delivery employing IMAP with bio-inspired MN array and without current application

Moreover, the combined effect of cone MA and ITP exhibits the deepest transdermal penetration, reaching ~2000 µm, as indicated in Figure 35. The implementation of ITP as a driving force further amplifies the model drug's permeation through the punctured skin model (agarose gel). Ultimately, the IMAP integrated with bio-inspired MA and ITP achieves a remarkable and synergistic enhancement in dye and acid delivery. The confluence of bio-inspired MA and ITP displays the deepest penetration depth, reaching ~2600 µm, as highlighted in Figure 36.

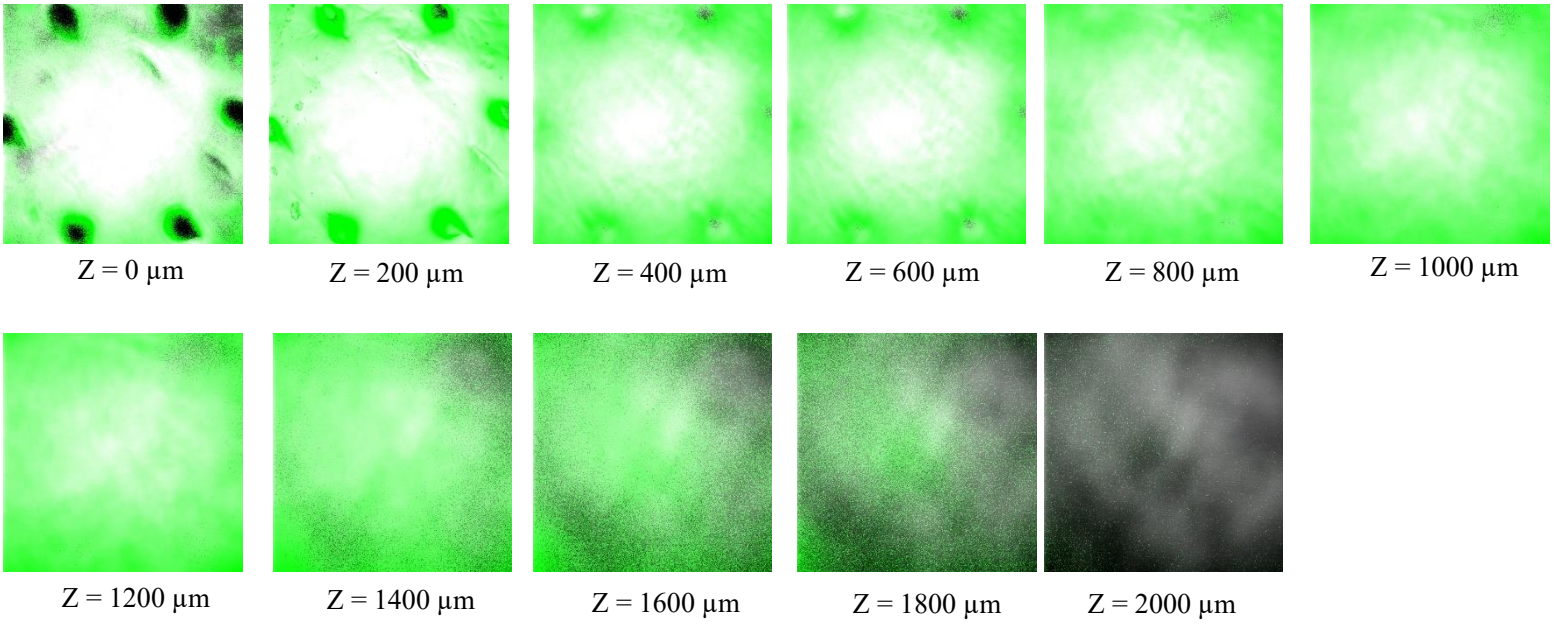


Figure 35: In vitro acid/dye delivery employing IMAP with cone MN array and with 1 mA current application ( 1mm )

The summary in Table 5 shows the diverse outcomes of in vitro acid/dye delivery across four distinct IMAP groups. To account for the inherent variability and inconsistencies observed in the depth of penetration across experimental replicates, we aim to illustrate this variability by employing error bars in Figure 37. These error bars serve as graphical representations of the extent of fluctuation and uncertainty within the dataset, portraying the dynamic nature of the results. The error bars on the graphs represent the standard deviations, which signify the variability or spread of data points around the mean value. For the in vitro studies, a sample size of 7 replicates was used, indicating that the experiments were repeated 7 times to ensure consistency and reliability of the results obtained in controlled laboratory conditions. This approach enhances the robustness and validity of the study's findings by incorporating sufficient replication. Notably, within this

Figure, the pivotal influence of both geometric variations and the role of ITP in facilitating the transfer process becomes evident, shedding light on the critical significance of these factors in the observed outcomes.

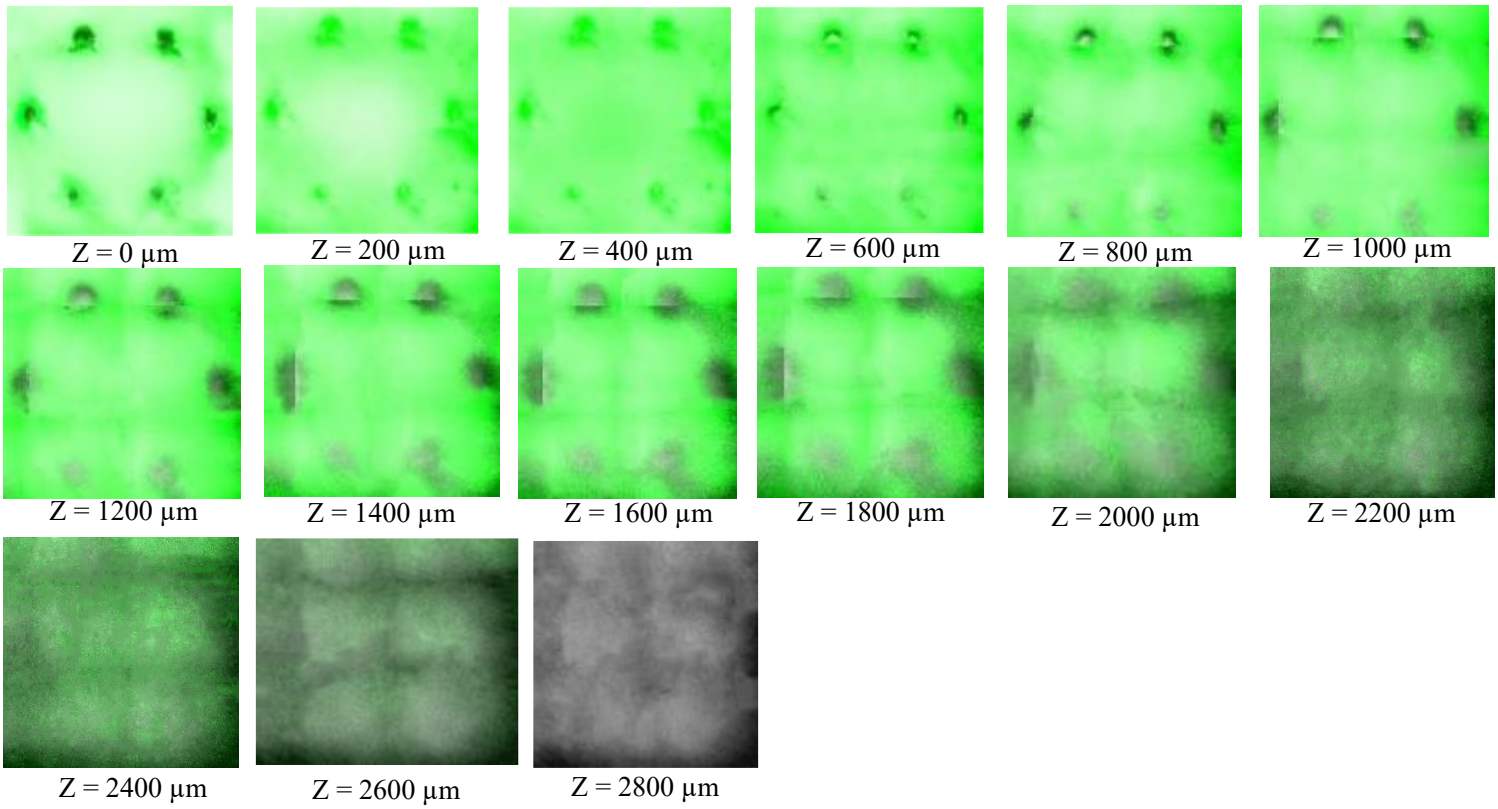


Figure 36: In vitro acid/dye delivery employing IMAP with bio-inspired MN array and with 1 mA current application ( 1mm )

This detailed investigation delineates the multi-faceted and synergistic enhancements achieved in delivery through the strategic integration of MAs and ITP, providing critical insights into their collaborative potential in effective drug diffusion through the skin layers.

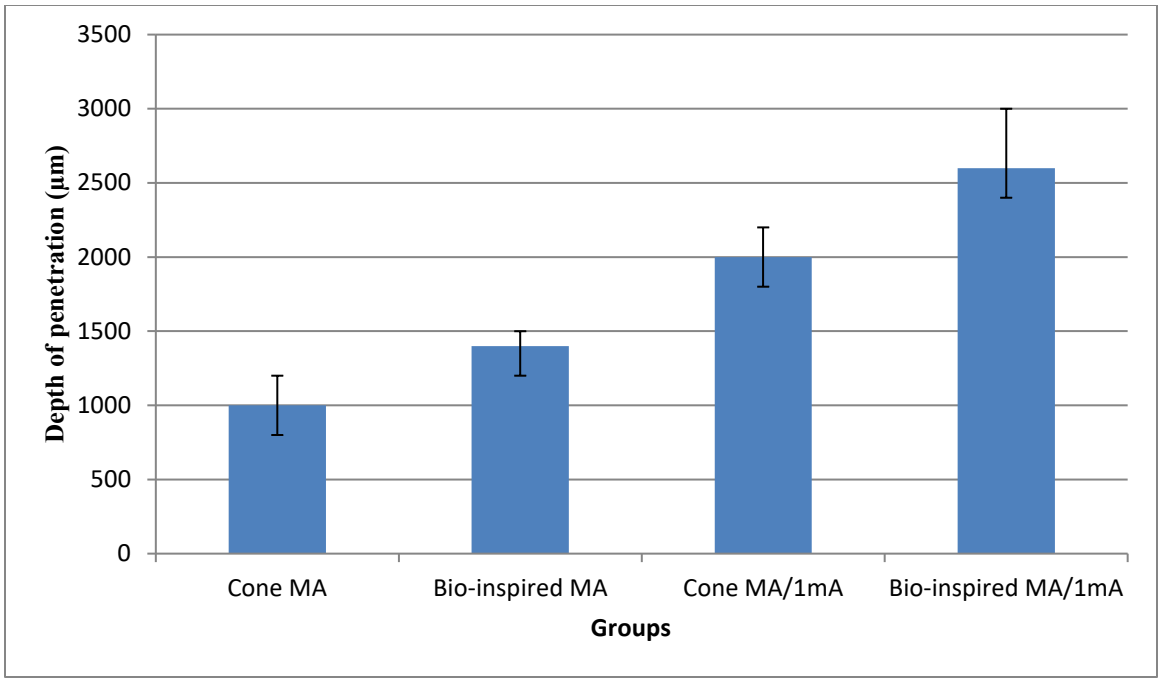


Figure 37: Depth of penetration for different IMAP groups

Table 5: Summary of depth of penetration for different IMAP groups

| | Depth of penetration [µm] |
|---|---|
| Cone MN without current for 10mins | 800-1200 |
| Bio-inspired MN without current for 10 mins | 1200-1500 |
| Cone MN and 1mA current for 10 mins | 1800-2200 |
| Bio-inspired MN and 1mA current for 10 mins | 2400-3000 |

# Chapter 5: Final remarks

## 5-1. Summary

This experimental study aimed to revolutionize drug delivery mechanisms by integrating bio-inspired MNs with ITP, emphasizing geometric modifications to enhance electric field, surface area, and volume within the delivery matrix. Computational analyses illustrated the superior performance of bio-inspired MNs over traditional cone-shaped variants, demonstrating enhanced drug concentrations within the skin.

Comparative analyses highlighted distinct impacts on drug delivery efficacy between bio-inspired and cone MN configurations. Bio-inspired MNs showed increased penetration depths and superior model drug delivery across skin model barriers, substantiated by fabrication and experimental validation.

The study focused on demonstrating the effectiveness of bio-inspired MNs in tandem with ITP to improve TDD. The distinct geometric features of these MNs, including barbs and well-defined edges, significantly amplified electric field strengths and heightened drug concentrations within the skin. Our initial aim was to integrate a greater number of barbs to potentially enhance their performance. However, attempts to fabricate MNs with more than five barbs resulted in unsatisfactory edges during the manufacturing process. Consequently, we established that restricting the barbs to five emerged as the optimal configuration for our 600 μm-high MN array. Moreover, MNs equipped with five uniformly sized barbs exhibited more pronounced and well-defined edges, a characteristic notably emphasized in the bio-inspired variants.

This research showcases a promising avenue for efficient and painless TDD, effectively overcoming skin barriers. The transformative potential unveiled warrants further exploration in medical applications, promising a paradigm shift in drug delivery systems.

The intricate process of MN fabrication using high-resolution 3D printing highlighted exceptional precision. Understanding skin anatomy enabled the development of an ingenious skin model, essential for conducting MN penetration tests.

Various experimental setups combining MNs with ITP revealed the profound impact of MN design on model drug diffusion and ITP effectiveness. The integration of MAs and ITP showcased remarkable improvements in model drug permeation rates through the gel barrier, demonstrating bio-inspired MNs' superior performance.

In summary, this study significantly contributes to understanding the synergy between MN designs and ITP in enhancing model drug diffusion through skin model. These findings offer promise for developing more effective drug delivery systems, potentially revolutionizing biomedical applications and advancing TDD technology.

## 5-2. Contribution

The research focuses on exploring the collaborative potential of bio-inspired MNs with ITP, aiming to enhance drug delivery across skin barriers. Transitioning from traditional cone-shaped MNs to bio-inspired variants, the study investigates improved model drug delivery efficiency by emphasizing increased penetration depth. Computational simulations using COMSOL Multiphysics 6.1 meticulously analyze key parameters, showcasing the superior performance of bio-inspired MNs with applied electrical currents. The thesis outlines this combination as a promising, efficient, and painless method for overcoming skin model barriers in model drug delivery.

Central to this investigation is the evaluation of bio-inspired MNs coupled with ITP for enhanced model drug delivery. Anticipated outcomes emphasize increased penetration depth over time, highlighting superior performance compared to cone MN arrays. Detailed findings offer insights into penetration dynamics, delving into MN design, skin anatomy, and charged particle movement within a gel matrix. The research segments systematically present comparative analyses between bio-inspired and cone MN configurations, showcasing the potential of bio-inspired MNs in augmenting model drug permeation rates and refining delivery mechanisms across skin model.

## 5-3. Future work

The future of bio-inspired MNs and ITP in drug delivery involves several key areas of advancement. One significant aspect is the refinement of MN design and fabrication. This includes optimizing barbed configurations to enhance adhesion, exploring new materials for improved performance, and developing manufacturing techniques for high precision and scalability.

In the realm of future research, a significant emphasis lies on conducting comprehensive in vitro assessments with skin, alongside in vivo investigations to authenticate the outcomes obtained from the laboratory experiments. The integration of multiple physical enhancement techniques holds promise for enhancing drug delivery efficiency, with the potential for testing various drug formulations.

It is proposed to conduct SEM analysis of the microneedles manufactured to assess their uniformity and size, thereby demonstrating the quality of the 3D-printed microneedles. Additionally, a strategy will be implemented to fabricate cross-sectional images of a subset of the microneedles to examine the manufacturing quality. Moreover, image processing techniques will be employed to generate 3D models from 2D cross-sectional images at various penetration depths. Furthermore, a comparative analysis between experimental and simulated results will be performed, utilizing both datasets interchangeably to refine and validate the simulation models.

Furthermore, it is imperative to prioritize the safety standards governing the production of microneedles, ensuring meticulous consideration of their mechanical robustness. A pivotal aspect involves assessing the fabricated microneedles for their durability to prevent any breakage upon insertion into the skin.

These forthcoming endeavors are geared towards enhancing the efficacy of bio-inspired microneedles (MNs) and iontophoresis (ITP) in drug delivery. The overarching objectives encompass refining the design parameters, optimizing drug delivery mechanisms, and extending the scope of applications across the healthcare landscape.

# References

[1] Y. Hao, W. Li, X. L. Zhou, F. Yang, and Z. Y. Qian, „Microneedles-based transdermal drug delivery systems: A review“, *J Biomed Nanotechnol*, vol. 13, no. 12, pp. 1581–1597, 2017, doi: 10.1166/jbn.2017.2474.

[2] R. Nagarkar, M. Singh, H. X. Nguyen, and S. Jonnalagadda, „A review of recent advances in microneedle technology for transdermal drug delivery“, *J Drug Deliv Sci Technol*, vol. 59, no. June, p. 101923, 2020, doi: 10.1016/j.jddst.2020.101923.

[3] A. J. Guillot, A. S. Cordeiro, R. F. Donnelly, M. C. Montesinos, T. M. Garrigues, and A. Melero, „Microneedle-based delivery: An overview of current applications and trends“, *Pharmaceutics*, vol. 12, no. 6, pp. 1–28, 2020, doi: 10.3390/pharmaceutics12060569.

[4] N. Elahpour, F. Pahlevanzadeh, M. Kharaziha, H. R. Bakhsheshi-Rad, S. Ramakrishna, and F. Berto, „3D printed microneedles for transdermal drug delivery: A brief review of two decades“, *Int J Pharm*, vol. 597, no. December 2020, p. 120301, 2021, doi: 10.1016/j.ijpharm.2021.120301.

[5] G. Ma and C. Wu, „Microneedle, bio-microneedle and bio-inspired microneedle: A review“, *Journal of Controlled Release*, vol. 251, pp. 11–23, 2017, doi: 10.1016/j.jconrel.2017.02.011.

[6] M. Azmana, S. Mahmood, A. R. Hilles, U. K. Mandal, K. A. Saeed Al-Japairai, and S. Raman, „Transdermal drug delivery system through polymeric microneedle: A recent update“, *J Drug Deliv Sci Technol*, vol. 60, no. June, p. 101877, 2020, doi: 10.1016/j.jddst.2020.101877.

[7] „Microneedle Systems for Vaccine Delivery: the story so far“

[8] F. Meng *et al.*, „Polymeric-based microneedle arrays as potential platforms in the development of drugs delivery systems“, *J Adv Res*, vol. 26, pp. 137–147, 2020, doi: 10.1016/j.jare.2020.07.017.

[9] X. He, J. Sun, J. Zhuang, H. Xu, Y. Liu, and D. Wu, „Microneedle System for Transdermal Drug and Vaccine Delivery: Devices, Safety, and Prospects“, *Dose-Response*, vol. 17, no. 4, pp. 1–18, 2019, doi: 10.1177/1559325819878585.

[10] S. Bhatnagar, P. R. Gadeela, P. Thathireddy, and V. V. K. Venuganti, „Microneedle-based drug delivery: materials of construction“, *Journal of Chemical Sciences*, vol. 131, no. 9, pp. 1–28, 2019, doi: 10.1007/s12039-019-1666-x.

[11] M. L. B. Queiroz *et al.*, „Microneedles as an alternative technology for transdermal drug delivery systems: a patent review“, *Expert Opin Ther Pat*, vol. 30, no. 6, pp. 433–452, 2020, doi: 10.1080/13543776.2020.1742324.

[12] F. Y. Wang, Y. Chen, Y. Y. Huang, and C. M. Cheng, „Transdermal drug delivery systems for fighting common viral infectious diseases“, *Drug Deliv Transl Res*, vol. 11, no. 4, pp. 1498–1508, 2021, doi: 10.1007/s13346-021-01004-6.

[13] A. McConville, C. Hegarty, and J. Davis, „Mini-Review: Assessing the Potential Impact of Microneedle Technologies on Home Healthcare Applications“, *Medicines*, vol. 5, no. 2, p. 50, 2018, doi: 10.3390/medicines5020050.

[14] S. Marshall, L. J. Sahm, and A. C. Moore, „The success of microneedle-mediated vaccine delivery into skin“, *Hum Vaccin Immunother*, vol. 12, no. 11, pp. 2975–2983, 2016, doi: 10.1080/21645515.2016.1171440.

[15] S. NAYAK, S. SURYAWANSHI, and V. BHASKAR, „Microneedle Technology for Transdermal Drug Delivery: Applications and Combination With Other Enhancing Techniques“, *Journal of Drug Delivery and Therapeutics*, vol. 6, no. 5, pp. 65–83, 2016, doi: 10.22270/jddt.v6i5.1285.

[16] N. Dragicevic and H. I. Maibach, *Percutaneous penetration enhancers physical methods in penetration enhancement*. 2017. doi: 10.1007/978-3-662-53273-7.

[17] Z. Luo, N. Paunović, and J. C. Leroux, „Physical methods for enhancing drug absorption from the gastrointestinal tract“, *Adv Drug Deliv Rev*, vol. 175, 2021, doi: 10.1016/j.addr.2021.05.024.

[18] D. D. Zhu, X. P. Zhang, B. L. Zhang, Y. Y. Hao, and X. D. Guo, „Safety Assessment of Microneedle Technology for Transdermal Drug Delivery: A Review“, *Adv Ther (Weinh)*, vol. 3, no. 8, pp. 1–14, 2020, doi: 10.1002/adtp.202000033.

[19] S. Dharadhar, A. Majumdar, S. Dhoble, and V. Patravale, „Microneedles for transdermal drug delivery: a systematic review“, *Drug Dev Ind Pharm*, vol. 45, no. 2, pp. 188–201, 2019, doi: 10.1080/03639045.2018.1539497.

[20] J. W. Lee and M. R. Prausnitz, „Drug delivery using microneedle patches: not just for skin“, *Expert Opin Drug Deliv*, vol. 15, no. 6, pp. 541–543, 2018, doi: 10.1080/17425247.2018.1471059.

[21] N. Khare and P. Shende, „Microneedle system: a modulated approach for penetration enhancement“, *Drug Dev Ind Pharm*, vol. 0, no. 0, pp. 1–10, 2021, doi: 10.1080/03639045.2021.1992421.

[22] R. S. Pawar, M. Dimri, A. Maithani, and K. Luv, „A Review of Microneedles – Elevation to TDDS Approach and Function in Management of Psoriasis“, *Asian Journal of Pharmaceutical Research and Development*, vol. 8, no. 6, pp. 77–80, 2020.

[23] D. Huang *et al.*, ‘A MINIMALLY INVASIVE IN VIVO ELECTROPORATION METHOD UTILIZING FLEXILE ELECTRODE AND MICRONEEDLE ROLLER National Key Laboratory of Science and Technology on Micro / Nano Fabrication , Institute of Microelectronics , Peking University , Beijing , China Inst’, pp. 1684–1687, 2017.

[24] S. NAYAK, S. SURYAWANSHI, and V. BHASKAR, ‘Microneedle Technology for Transdermal Drug Delivery: Applications and Combination With Other Enhancing Techniques’, *Journal of Drug Delivery and Therapeutics*, vol. 6, no. 5, pp. 65–83, 2016, doi: 10.22270/jddt.v6i5.1285.

[25] K. B. Vinayakumar, K. Rajanna, N. S. Dinesh, and M. M. Nayak, ‘Out-of-plane cup shaped stainless steel microneedle array for drug delivery’, *2016 IEEE 11th Annual International Conference on Nano/Micro Engineered and Molecular Systems, NEMS 2016*, pp. 172–175, 2016, doi: 10.1109/NEMS.2016.7758225.

[26] Y. Mizuno *et al.*, ‘Fabrication of novel-shaped microneedles to overcome the disadvantages of solid microneedles for the transdermal delivery of insulin’, *Biomed Microdevices*, vol. 23, no. 3, 2021, doi: 10.1007/s10544-021-00576-x.

[27] L. Lin *et al.*, ‘Multimicrochannel Microneedle Microporation Platform for Enhanced Intracellular Drug Delivery’, *Adv Funct Mater*, vol. 32, no. 21, pp. 1–13, 2022, doi: 10.1002/adfm.202109187.

[28] W. G. Bae *et al.*, ‘Snake fang-inspired stamping patch for transdermal delivery of liquid formulations’, *Sci Transl Med*, vol. 11, no. 503, pp. 1–12, 2019, doi: 10.1126/scitranslmed.aaw3329.

[29] M. Yang, J.D. Zahn, Microneedle insertion force reduction using vibratory actuation, Biomed. Microdevices 6 (2004) 177–182.

[30] X.Q. Kong, Study on Mechanics Behaviors of Mosquito's Floating and AcupuncturingThesis (PhD) Dalian University of Technology, China, 2010.

[31] J.C. Wang, Coupling Bionic Research on Painless Injector Needles Based on Insect Piercing-sucking MouthpartThesis (PhD) Jilin University, China, 2008.

[32] Tran, Le-Giang, Thanh-Qua Nguyen, and Woo-Tae Park. "Bio-inspired barbed microneedle for skin adhesion with interlocking mechanics." *2019 IEEE 32nd International Conference on Micro Electro Mechanical Systems (MEMS)*. IEEE, 2019.

[33] Chen Z, Lin Y, Lee W, Ren L, Liu B, Liang L, Wang Z and Jiang L 2018 Additive Manufacturing of Honeybee-Inspired Microneedle for Easy Skin Insertion and Difficult Removal *ACS Appl. Mater.Interfaces* 10 29338–46

[34] Karp J M and Langer R 2011 Materials science: dry solution to a sticky problem *Nature* 477 42

[35] Koh L-D, Cheng Y, Teng C-P, Khin Y-W, Loh X-J, Tee S-Y, Low M, Ye E, Yu H-D and Zhang Y-W 2015 Structures, mechanical properties and applications of silk fibroin materials *Prog. Polym. Sci.* 46 86–110

[36] Moon Kyu Kwak, Hoon-Eui Jeong, Kahp Y. Suh," Rational Design and Enhanced Biocompatibility of a Dry Adhesive Medical Skin", *Advanced Materials*, 23(34), pp. 3949-3953, 2011

[37] Yun Yang, Eoin D. O'Cearbhaill, Geoffroy C. Sisk, Kyeng Min Park, Woo Kyung Cho, Martin Villiger, Brett E. Bouma, Bohdan Pomahac, and Jeffrey M. Karp, "A bioinspired swellable microneedle adhesive for mechanical interlocking with tissue", *Nature communications*, 4(1702), 2013

[38] Woo Kyung Cho, James A. Ankrum and Jeffrey M., "Micro structured barbs on the North American porcupine quill enable easy tissue penetration and difficult removal", *Proceedings of the National Academy of Sciences of the United States of America*, **109**(52), pp.21289-21294, **2012**

[39] Morde, Riddish Sudhir. *Micro-3D printing of bio-inspired microneedle with enhanced adhesion capabilities*. Diss. Rutgers University-School of Graduate Studies, 2018.

[40] A. K. Banga, S. Bose, and T. K. Ghosh, 'Iontophoresis and electroporation: Comparisons and contrasts', *Int J Pharm*, vol. 179, no. 1, pp. 1–19, 1999, doi: 10.1016/S0378-5173(98)00360-3.

[41] D. Huang *et al.*, 'Efficient delivery of nucleic acid molecules into skin by combined use of microneedle roller and flexible interdigitated electroporation array', *Theranostics*, vol. 8, no. 9, pp. 2361–2376, 2018, doi: 10.7150/thno.23438.

[42] A. K. Banga, S. Bose, and T. K. Ghosh, 'Iontophoresis and electroporation: Comparisons and contrasts', *Int J Pharm*, vol. 179, no. 1, pp. 1–19, 1999, doi: 10.1016/S0378-5173(98)00360-3.

[43] J. Yang *et al.*, 'Smartphone-powered iontophoresis-microneedle array patch for controlled transdermal delivery', *Microsyst Nanoeng*, vol. 6, no. 1, 2020, doi: 10.1038/s41378-020-00224-z.

[44] D. Xia, R. Jin, G. Byagathvalli, H. Yu, L. Ye, and C. Lu, 'An ultra-low-cost electroporator with microneedle electrodes ( ePatch ) for SARS-CoV-2 vaccination', vol. 118, no. 45, 2021, doi: 10.1073/pnas.2110817118/-/DCSupplemental.Published.

[45] S. Xiao, Y. Yan, J. Zhao, Y. Zhang, and N. Feng, 'Increased microneedle-mediated transdermal delivery of tetramethylpyrazine to the brain, combined with borneol and iontophoresis, for MCAO prevention', *Int J Pharm*, vol. 575, no. August 2019, 2020, doi: 10.1016/j.ijpharm.2019.118962.

[46] P. Surgery, 'In vivo HPLC tissue concentration study of three drugs (caffeine, biotin and procaine) administered by microneedling, electroporation and both techniques combined', vol. 2, no. 4, 2016.

[47] T. Yang *et al.*, 'Rolling microneedle electrode array (RoMEA) empowered nucleic acid delivery and cancer immunotherapy', *Nano Today*, vol. 36, p. 101017, 2021, doi: 10.1016/j.nantod.2020.101017.

[48] C. O'Mahony, R. Houlihan, K. Grygoryev, Z. Ning, J. Williams, and T. Moore, 'Design, modelling and preliminary characterisation of microneedle-based electrodes for tissue electroporation in vivo', *J Phys Conf Ser*, vol. 757, no. 1, 2016, doi: 10.1088/1742-6596/757/1/012040.

[49] M. Bok *et al.*, 'Microneedles integrated with a triboelectric nanogenerator: An electrically active drug delivery system', *Nanoscale*, vol. 10, no. 28, pp. 13502–13510, 2018, doi: 10.1039/c8nr02192a.

[50] A. Wanasathop and S. Kevin Li, 'Iontophoretic drug delivery in the oral cavity', *Pharmaceutics*, vol. 10, no. 3, pp. 1–17, 2018, doi: 10.3390/pharmaceutics10030121.

[51] V. L. Perez, B. Wirostko, M. Korenfeld, S. From, and M. Raizman, 'Ophthalmic drug delivery using iontophoresis: Recent clinical applications', *Journal of Ocular Pharmacology and Therapeutics*, vol. 36, no. 2, pp. 75–87, 2020, doi: 10.1089/jop.2019.0034.

[52] M. Abbasi, Z. Fan, J. A. Dawson, and S. Wang, 'Transdermal Delivery of Metformin Using Dissolving Microneedles and Iontophoresis Patches for Browning Subcutaneous Adipose Tissue', *Pharmaceutics*, vol. 14, no. 4, 2022, doi: 10.3390/pharmaceutics14040879.

[53] D. Vora, H. T. Garimella, C. L. German, and A. K. Banga, 'Microneedle and iontophoresis mediated delivery of methotrexate into and across healthy and psoriatic skin', *Int J Pharm*, vol. 618, no. December 2021, 2022, doi: 10.1016/j.ijpharm.2022.121693.

[54] J. H. Jung, B. Chiang, H. E. Grossniklaus, and M. R. Prausnitz, 'Ocular drug delivery targeted by iontophoresis in the suprachoroidal space using a microneedle', *Journal of Controlled Release*, vol. 277, no. November 2017, pp. 14–22, 2018, doi: 10.1016/j.jconrel.2018.03.001.

[55] A. A. Dandekar, H. T. Garimella, C. L. German, and A. K. Banga, 'Microneedle Mediated Iontophoretic Delivery of Tofacitinib Citrate', *Pharm Res*, no. 0123456789, 2022, doi: 10.1007/s11095-022-03190-5.

[56] M. S. A. Junaid and A. K. Banga, 'Transdermal Delivery of Baclofen Using Iontophoresis and Microneedles', *AAPS PharmSciTech*, vol. 23, no. 3, pp. 1–8, 2022, doi: 10.1208/s12249-022-02232-w.

[57] Y. Li *et al.*, 'Iontophoresis-driven porous microneedle array patch for active transdermal drug delivery', *Acta Biomater*, vol. 121, pp. 349–358, 2021, doi: 10.1016/j.actbio.2020.12.023.

[58] S. Kusama *et al.*, 'Transdermal electroosmotic flow generated by a porous microneedle array patch', *Nat Commun*, vol. 12, no. 1, 2021, doi: 10.1038/s41467-021-20948-4.

[59] X. Li *et al.*, 'A Fully Integrated Closed-Loop System Based on Mesoporous Microneedles-Iontophoresis for Diabetes Treatment', *Advanced Science*, vol. 8, no. 16, pp. 1–15, 2021, doi: 10.1002/advs.202100827.

[60] J. P. Ronnander, L. Simon, and A. Koch, 'Transdermal Delivery of Sumatriptan Succinate Using Iontophoresis and Dissolving Microneedles', *J Pharm Sci*, vol. 108, no. 11, pp. 3649–3656, 2019, doi: 10.1016/j.xphs.2019.07.020.

[61] G. Noh *et al.*, 'Iontophoretic transdermal delivery of human growth hormone (hGH) and the combination effect of a new type microneedle, tappy tok tok®', *Pharmaceutics*, vol. 10, no. 3, 2018, doi: 10.3390/pharmaceutics10030153.

[62] B. Chen, J. Wei, and C. Iliescu, 'Sonophoretic enhanced microneedles array (SEMA)—Improving the efficiency of transdermal drug delivery', *Sens Actuators B Chem*, vol. 145, no. 1, pp. 54–60, Mar. 2010, doi: 10.1016/j.snb.2009.11.013.

[63] T. Han and D. B. Das, 'Permeability Enhancement for Transdermal Delivery of Large Molecule Using Low-Frequency Sonophoresis Combined with Microneedles', *J Pharm Sci*, vol. 102, no. 10, pp. 3614–3622, Oct. 2013, doi: 10.1002/jps.23662.

[64] Z. Chen *et al.*, '3D-Printed Integrated Ultrasonic Microneedle Array for Rapid Transdermal Drug Delivery', *Mol Pharm*, vol. 19, no. 9, pp. 3314–3322, Sep. 2022, doi: 10.1021/acs.molpharmaceut.2c00466.

[65] I. de J. Martínez-Segoviano and A. Ganem-Rondero, 'Enhancement of the transdermal delivery of zidovudine by pretreating the skin with two physical enhancers: microneedles and sonophoresis', *DARU, Journal of Pharmaceutical Sciences*, vol. 29, no. 2, pp. 279–290, Dec. 2021, doi: 10.1007/s40199-021-00402-y.

[66] A. Nayak, H. Babla, T. Han, and D. B. Das, 'Lidocaine carboxymethylcellulose with gelatine co-polymer hydrogel delivery by combined microneedle and ultrasound', *Drug Deliv*, vol. 23, no. 2, pp. 668–679, Feb. 2016, doi: 10.3109/10717544.2014.935985.

[67] Y. C. Ryu, D. I. Kim, S. H. Kim, H. M. D. Wang, and B. H. Hwang, 'Synergistic Transdermal Delivery of Biomacromolecules Using Sonophoresis after Microneedle Treatment', *Biotechnology and Bioprocess Engineering*, vol. 23, no. 3, pp. 286–292, Jun. 2018, doi: 10.1007/s12257-018-0070-6.

[68] X. Ning *et al.*, 'Photodynamic Bubble-Generating Microneedles for Enhanced Transdermal Cancer Therapy', *ACS Appl Polym Mater*, vol. 3, no. 12, pp. 6502–6512, Dec. 2021, doi: 10.1021/acsapm.1c01219.

[69] S. Shao *et al.*, 'Layer-by-Layer Assembly of Lipid Nanobubbles on Microneedles for Ultrasound-Assisted Transdermal Drug Delivery', *ACS Appl Bio Mater*, vol. 5, no. 2, pp. 562–569, Feb. 2022, doi: 10.1021/acsabm.1c01049.

[70] Y. Yang, L. Xia, X. Ning, T. Hu, C. Xu, and W. Liu, 'Enhanced Drug Permeation into Human Keloid Tissues by Sonophoresis-Assisted Microneedling', *SLAS Technol*, vol. 26, no. 6, pp. 660–666, Dec. 2021, doi: 10.1177/24726303211024568.

[71] A. Zandi *et al.*, 'Microneedle-Based Generation of Microbubbles in Cancer Tumors to Improve Ultrasound-Assisted Drug Delivery', *Adv Healthc Mater*, vol. 8, no. 17, Sep. 2019, doi: 10.1002/adhm.201900613.

[72] M. A. Lopez-Ramirez *et al.*, 'Built-In Active Microneedle Patch with Enhanced Autonomous Drug Delivery', *Advanced Materials*, vol. 32, no. 1, p. 1905740, Jan. 2020, doi: 10.1002/adma.201905740.

[73] M. C. Chen, Z. W. Lin, and M. H. Ling, 'Near-infrared light-activatable microneedle system for treating superficial tumors by combination of chemotherapy and photothermal therapy', *ACS Nano*, vol. 10, no. 1, pp. 93–101, Jan. 2016, doi: 10.1021/acsnano.5b05043.

[74] Y. Sun *et al.*, 'Self-assembly nanomicelle-microneedle patches with enhanced tumor penetration for superior chemo-photothermal therapy', *Nano Res*, vol. 15, no. 3, pp. 2335–2346, Mar. 2022, doi: 10.1007/s12274-021-3817-x.

[75] W. Qin *et al.*, 'Dissolving microneedles with spatiotemporally controlled pulsatile release nanosystem for synergistic chemo-photothermal therapy of Melanoma', *Theranostics*, vol. 10, no. 18, pp. 8179–8196, 2020, doi: 10.7150/thno.44194.

[76] W. Yu *et al.*, 'Build an implanted "arsenal": Detachable microneedles for NIR-triggered cancer photothermo-chemotherapy', *Biomater Sci*, vol. 9, no. 13, pp. 4737–4745, Jul. 2021, doi: 10.1039/d1bm00520k.

[77] J. Chen *et al.*, 'A responsive microneedle system for efficient anti-melanoma by combining self-enhanced chemodynamic therapy with photothermal therapy', *Chemical Engineering Journal*, vol. 431, Mar. 2022, doi: 10.1016/j.cej.2021.133466.

[78] Y. Gao *et al.*, 'Transdermal delivery of therapeutics through dissolvable gelatin/sucrose films coated on PEGDA microneedle arrays with improved skin permeability', *J Mater Chem B*, vol. 7, no. 47, pp. 7515–7524, 2019, doi: 10.1039/c9tb01994d.

[79] L. Dong *et al.*, 'Au Nanocage-Strengthened Dissolving Microneedles for Chemo-Photothermal Combined Therapy of Superficial Skin Tumors', *ACS Appl Mater Interfaces*, vol. 10, no. 11, pp. 9247–9256, Mar. 2018, doi: 10.1021/acsami.7b18293.

[80] Y. Zhao *et al.*, 'Intelligent and spatiotemporal drug release based on multifunctional nanoparticle-integrated dissolving microneedle system for synergetic chemo-photothermal therapy to eradicate melanoma', *Acta Biomater*, vol. 135, pp. 164–178, Nov. 2021, doi: 10.1016/j.actbio.2021.09.009.

[81] T. Peng *et al.*, 'Dissolving Microneedles Loading TPGS Biphasic Functionalized PLGA Nanoparticles for Efficient Chemo-Photothermal Combined Therapy of Melanoma', *Adv Ther (Weinh)*, vol. 3, no. 6, p. 1900190, Jun. 2020, doi: 10.1002/adtp.201900190.

[82]T. Peng *et al.*, 'TPGS/hyaluronic acid dual-functionalized PLGA nanoparticles delivered through dissolving microneedles for markedly improved chemo-photothermal combined therapy of superficial tumor', *Acta Pharm Sin B*, vol. 11, no. 10, pp. 3297–3309, Oct. 2021, doi: 10.1016/j.apsb.2020.11.013.

[83] M. Yang and J. D. Zahn, 'Microneedle Insertion Force Reduction Using Vibratory Actuation', *Biomed Microdevices*, vol. 6, no. 3, pp. 177–182, Sep. 2004, doi: 10.1023/B:BMMD.0000042046.07678.2e.

[84] H. Izumi *et al.*, 'Combined Harpoonlike Jagged Microneedles Imitating Mosquito's Proboscis and Its Insertion Experiment with Vibration', *IEEJ Transactions on Electrical and Electronic Engineering*, vol. 3, no. 4, pp. 425–431, Jul. 2008, doi: 10.1002/tee.20295.

[85] F.-W. Lee, W.-H. Hung, C.-W. Ma, and Y.-J. Yang, ‘Polymer-based disposable microneedle array with insertion assisted by vibrating motion’, *Biomicrofluidics*, vol. 10, no. 1, p. 011905, Jan. 2016, doi: 10.1063/1.4939948.

[86] M. Suzuki, T. Takahashi, and S. Aoyagi, ‘3D laser lithographic fabrication of hollow microneedle mimicking mosquitos and its characterisation’, *Int J Nanotechnol*, vol. 15, no. 1/2/3, p. 157, 2018, doi: 10.1504/IJNT.2018.089545.

[87] J. Kim, S. Park, G. Nam, Y. Choi, S. Woo, and S. H. Yoon, ‘Bioinspired microneedle insertion for deep and precise skin penetration with low force: Why the application of mechanophysical stimuli should be considered’, *J Mech Behav Biomed Mater*, vol. 78, pp. 480–490, Feb. 2018, doi: 10.1016/j.jmbbm.2017.12.006.

[88] T. Kang *et al.*, ‘The synergistic effect of mechanical vibration for skin puncturing using polymeric microneedles’, *J Drug Deliv Sci Technol*, vol. 71, May 2022, doi: 10.1016/j.jddst.2022.103334.

[89] T. T. Liu, K. Chen, and Q. Wang, ‘Skin drug permeability and safety through a vibrating solid micro-needle system’, *Drug Deliv Transl Res*, vol. 8, no. 5, pp. 1025–1033, Oct. 2018, doi: 10.1007/s13346-018-0544-2.

[90] C. A. Lee, J. S. Baek, D. G. Kwag, H. J. Lee, J. Park, and C. W. Cho, ‘Enhancement of skin permeation of vitamin C using vibrating microneedles’, *Transl Clin Pharmacol*, vol. 25, no. 1, pp. 15–20, 2017, doi: 10.12793/tcp.2017.25.1.15.

[91] V. R. Jayaneththi, K. Aw, M. Sharma, J. Wen, D. Svirskis, and A. J. McDaid, ‘Controlled transdermal drug delivery using a wireless magnetic microneedle patch: Preclinical device development’, *Sens Actuators B Chem*, vol. 297, Oct. 2019, doi: 10.1016/j.snb.2019.126708.

[92] X. Zhang, G. Chen, X. Fu, Y. Wang, and Y. Zhao, ‘Magneto-Responsive Microneedle Robots for Intestinal Macromolecule Delivery’, *Advanced Materials*, vol. 33, no. 44, Nov. 2021, doi: 10.1002/adma.202104932.

[93] J. Lee, H. Lee, S. hyun Kwon, and S. Park, ‘Active delivery of multi-layer drug-loaded microneedle patches using magnetically driven capsule’, *Med Eng Phys*, vol. 85, pp. 87–96, Nov. 2020, doi: 10.1016/j.medengphy.2020.09.012.

[94] J. Lee, S. W. Sohn, H. Lee, and S. Park, ‘Open-close Mechanism of Magnetically Actuated Capsule for Multiple Hemostatic Microneedle Patch Delivery’, *Int J Control Autom Syst*, vol. 20, no. 7, pp. 2285–2296, Jul. 2022, doi: 10.1007/s12555-021-0306-7.

[95] M. Bok, Z.-J. Zhao, S. Jeon, J.-H. Jeong, and E. Lim, ‘Ultrasonically and Iontophoretically Enhanced Drug-Delivery System Based on Dissolving Microneedle Patches’, *Sci Rep*, vol. 10, no. 1, p. 2027, Feb. 2020, doi: 10.1038/s41598-020-58822-w.

[96] J. Yang et al., “Touch-actuated microneedle array patch for closed-loop transdermaldrug delivery,” Drug Deliv., vol. 25, no. 1, pp. 1728–1739, 2018.

[97] Huang, Jigang, Qin Qin, and Jie Wang. "A review of stereolithography: Processes and systems." Processes 8.9 (2020): 1138.

[98] Montagna, William and Ebling, F. John G.. "human skin". Encyclopedia Britannica, 18 Mar. 2023, https://www.britannica.com/science/human-skin. Accessed 4 April 2023.